



**HAL**  
open science

# Accuracy of Potfit-based potential representations and its impact on the performance of (ML-)MCTDH

Frank Otto, Ying-Chih Chiang, Daniel Peláez

► **To cite this version:**

Frank Otto, Ying-Chih Chiang, Daniel Peláez. Accuracy of Potfit-based potential representations and its impact on the performance of (ML-)MCTDH. *Chemical Physics*, 2018, 509, pp.116-130. 10.1016/j.chemphys.2017.11.013 . hal-01852004

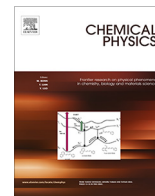
**HAL Id: hal-01852004**

**<https://hal.science/hal-01852004>**

Submitted on 15 Jul 2024

**HAL** is a multi-disciplinary open access archive for the deposit and dissemination of scientific research documents, whether they are published or not. The documents may come from teaching and research institutions in France or abroad, or from public or private research centers.

L'archive ouverte pluridisciplinaire **HAL**, est destinée au dépôt et à la diffusion de documents scientifiques de niveau recherche, publiés ou non, émanant des établissements d'enseignement et de recherche français ou étrangers, des laboratoires publics ou privés.



# Accuracy of Potfit-based potential representations and its impact on the performance of (ML-)MCTDH

Frank Otto<sup>a,\*</sup>, Ying-Chih Chiang<sup>b</sup>, Daniel Peláez<sup>c</sup>

<sup>a</sup>Dept. of Chemistry, University College London, 20 Gordon St., London WC1H 0AJ, UK

<sup>b</sup>Dept. of Physics, The Chinese University of Hong Kong, Sha Tin, N.T., Hong Kong

<sup>c</sup>Laboratoire de Physique des Lasers, Atomes et Molécules (PhLAM), Unité Mixte de Recherche (UMR) 8523, Université Lille 1, Bât. P5, Villeneuve d'Ascq Cedex, France

## ARTICLE INFO

### Article history:

Received 22 September 2017

In final form 20 November 2017

Available online 21 November 2017

### Keywords:

Quantum molecular dynamics

MCTDH

Potential energy surfaces

Monte Carlo methods

## ABSTRACT

Quantum molecular dynamics simulations with MCTDH or ML-MCTDH perform best if the potential energy surface (PES) has a sum-of-products (SOP) or multi-layer operator (MLOp) structure. Here we investigate four different POTFIT-based methods for representing a general PES as such a structure, among them the novel random-sampling multi-layer Potfit (RS-MLPF). We study how the format and accuracy of the PES representation influences the runtime of a benchmark (ML-)MCTDH calculation, namely the computation of the ground state of the  $\text{H}_3\text{O}_2^-$  ion. Our results show that compared to the SOP format, the MLOp format leads to a much more favorable scaling of the (ML-)MCTDH runtime with the PES accuracy. At reasonably high PES accuracy, ML-MCTDH calculations thus become up to 20 times faster, and taken to the extreme, the RS-MLPF method yields extremely accurate PES representations (global root-mean-square error of  $\sim 0.1 \text{ cm}^{-1}$ ) which still lead to only moderate computational demands for ML-MCTDH.

© 2017 Elsevier B.V. All rights reserved.

## 1. Introduction

The computational treatment of high-dimensional quantum systems unavoidably necessitates the use of approximations, given the currently available hardware facilities. These approximations include the discretization of the Hilbert space (using grid-based or basis-set methods), the representation of the wavefunction, and the time-stepping method (for dynamical problems). In the case of quantum molecular dynamics (QMD), which is usually carried out in the framework of the Born-Oppenheimer or (in the case of several electronic states) group Born-Oppenheimer approximations [1], further approximations are introduced by the creation of one or more potential energy surfaces (PES) on which the nuclei move, which involves the level of electronic structure theory, the electronic basis set, and how the computed electronic energies are fitted to a global function. Moreover, to make use of such a PES in the QMD calculations, further approximating transformations of the PES may be needed. Alternatively, promising on-the-fly QMD methods are available as well [2,3], though the computational effort in the electronic structure calculations still limits their general applicability. In all these approximation steps, the balance

between accuracy and computational resource usage must be considered, and it is worth noting that different approximation methods exhibit different scalings between approximation accuracy and resource usage. Since researchers are usually faced with limited computational budgets, ideally the approximation methods should be chosen such that resource usage is minimized for a given desired accuracy.

Concerning the representation of the wavefunction, major breakthroughs in obtaining accurate results with limited resources were achieved by Meyer and coworkers in developing the multi-configuration time-dependent Hartree method (MCTDH) [4–7]. MCTDH has proven to be a powerful computational method for high-dimensional quantum systems, both for investigating the system dynamics [8–14] as well as for determining spectroscopic features [15,16,11,17–22], where it should be noted that the list of cited works is far from complete. With its multi-layer extension ML-MCTDH [23–25], accurate full-dimensional quantum calculations for systems with up to hundreds of degrees of freedom (DOFs) are possible [23,26–30,25,31–33]. From the approximation perspective, (ML-)MCTDH is particularly attractive as it allows to systematically increase the accuracy by increasing the size of the wavefunction representation, at the expense of using more computational resources. In this respect ML-MCTDH fares better than

\* Corresponding author.

E-mail address: [oft.kontra@gmail.com](mailto:oft.kontra@gmail.com) (F. Otto).

MCTDH, as resource usage depends only polynomially instead of exponentially on the wavefunction size [24,34].

A crucial point for the efficient application of (ML-)MCTDH is that the PES needs to be represented in a suitable format which facilitates the efficient evaluation of the various high-dimensional integrals that are encountered in the course of the (ML-)MCTDH algorithm. This requirement can be overcome by using the CDVR method [35,36] which however requires a very large amount of PES evaluations, and considerable development effort may be needed to overcome the resulting bottleneck by massively speeding up the PES routine [37]. In general it is much more economical to represent the PES as a sum of products of one- or low-dimensional potential functions, an approach that has been traditionally used with MCTDH, as it transforms each high-dimensional integral into a sum of products of one- or low-dimensional integrals, which are easily evaluated. This sum-of-products (SOP) format is a suitable choice for ML-MCTDH as well [24]. More recently, one of the authors has shown that for ML-MCTDH there exists an alternative representation of the PES as a *hierarchical* sum of products, i.e. as a *multi-layer operator* (MLOp), which allows for a much more compact representation of the PES and hence for a much more efficient evaluation of the ML-MCTDH equations of motion [34].

For most model systems, the PES can be naturally expressed in SOP format. However, general PES are usually given as a high-dimensional analytic function fitted to a large number of electronic structure calculations, and for such PES it is necessary to transform them into SOP or MLOp format. In general, it is not possible to perform this transformation exactly, but only approximately; and more accurate representations of the PES unavoidably lead to a larger number of terms in the representation, which negatively impacts the performance of (ML-)MCTDH (e.g. for the SOP format, the computational effort for MCTDH is directly proportional to the number of summands in the expansion). Given a desired accuracy of the PES representation, one should then strive to find a PES representation which minimizes the effort for (ML-)MCTDH.

There are a number of options for performing this transformation, most of them targeting the SOP format. One such approach makes use of neural networks with exponential activation functions [38–42] but so far this method has only been demonstrated for fitting functions up to 6D (i.e. up to four atoms). Another approach is the  $n$ -mode representation ( $n$ -MR) [43], also known as cut high-dimensional model representation (cut-HDMR) [44], which expands the PES as a sum of one- and few-body terms, and the latter can be transformed into SOP format relatively easily. This method can scale to rather large systems, and it has been used in MCTDH calculations e.g. on the Zundel cation [45,16,11,17,46] as well as on malonaldehyde [18], and it has also been used together with the neural networks approach [47]. However, the drawback of the  $n$ -MR approach is that the number of terms grows exponentially with the expansion order, so that for larger systems one must choose (usually using statistical methods) the most relevant terms in the  $n$ -MR expansion. This makes the method non-variational, i.e. adding more terms to the expansion does not necessarily increase its accuracy, so that it is difficult to obtain a PES fit with a prescribed accuracy. Furthermore, it has been shown that this non-variational behaviour may lead to artificial structure in the PES [48]. In contrast, the Potfit method [49] offers good control over the accuracy of the SOP fit, as it is variational. Given the values of the PES on a product grid, Potfit determines optimal one-dimensional potential functions for each DOF, and expresses the PES as a linear combination of products of these potential functions (technically, a truncated Tucker decomposition [50]), which results in a SOP expansion close to optimal. However, the requirement of knowing the PES on a full product grid limits the applicability of Potfit to systems with 6–8 DOFs. This limitation can be overcome by approximating the integrations over the full grid by multi-grid

or Monte Carlo methods, giving rise to the multi-grid Potfit (MGPF) [51] and the Monte Carlo Potfit (MCPF) [52] methods, respectively. MGPF is expected to be able to treat PES up to 12D, while MCPF has already been applied to a 15D PES, though with considerable computational effort. On the other hand, for transforming a PES into MLOp format there currently exists to our knowledge only one method, multi-layer Potfit (MLPF) [34], which is based on the hierarchical singular value decomposition [53]. As initially conceived, MLPF like Potfit requires knowing the PES on a full product grid, limiting its applicability. To overcome this problem, the present article introduces a novel method for transforming a PES into MLOp form, which avoids having to evaluate the PES on the full product grid by using ideas originally introduced in MCPF [52]. The resulting method is termed “random sampling multi-layer Potfit” (RS-MLPF), and by design we expect it to scale to systems as large as those treatable by MCPF and likely beyond.

In the present work, we aim to investigate how the accuracy of the PES fit into SOP/MLOp format influences the runtime of (ML-)MCTDH calculations carried out with this fit. For this purpose we have chosen the  $\text{H}_3\text{O}_2^-$  ion as a benchmark system, for which we compute the ground state and its zero-point energy using relaxation methods. This 9-dimensional (9D) system is slightly too large to be treated with the original Potfit method, but PES fits suitable for (ML-)MCTDH can be obtained with the aforementioned improved Potfit variants. In particular, we use four such variants in our calculations: (i) MGPF, (ii) MGPF postprocessed by MLPF, (iii) MLPF directly, and (iv) the newly developed RS-MLPF. For each variant, we produce a series of PES fits at different accuracy levels, and measure the resulting runtime for the (ML-)MCTDH relaxation. The accuracy of each fit is assessed by sampling the fitting error with Monte Carlo as well as classical molecular dynamics methods. Our results reveal that the choice of Potfit variant can have a strong influence on the computational resource usage of (ML-)MCTDH, especially when a highly accurate PES fit is required.

The article is structured as follows: Section 2 reviews the methods used in this study. In particular, Section 2.3 gives details on the novel RS-MLPF method. Section 3 describes some properties of the  $\text{H}_3\text{O}_2^-$  ion and the PES used. Our calculations and their results are given in Section 4. Section 5 concludes. Appendix A details our error estimation procedure for the PES fits. As a help to the reader, Table 1 lists the acronyms used frequently in this article.

## 2. Methodological background

### 2.1. MCTDH, ML-MCTDH, and form of the Hamiltonian

The multi-configuration time-dependent Hartree (MCTDH) method [4–7] and its multi-layer variant (ML-MCTDH) [23–25] have been widely discussed in detail elsewhere. Here we only review a few key concepts of these methods, as far as they are relevant for the present investigation.

MCTDH derives its efficiency from a compact representation of the wavefunction, which reads

$$\Psi(q_1, \dots, q_f, t) = \sum_{j_1=1}^{n_1} \dots \sum_{j_f=1}^{n_f} A_{j_1 \dots j_f}(t) \varphi_{j_1}^{(1)}(q_1, t) \dots \varphi_{j_f}^{(f)}(q_f, t) \quad (1)$$

where  $f$  denotes the number of degrees of freedom (DOFs) of the system,  $q_1$  through  $q_f$  are the system coordinates,  $t$  is the time,  $n_1$  through  $n_f$  are expansion orders, and  $A$  is a vector of coefficients (the so-called “ $A$ -vector”). The “single-particle functions” (SPFs)  $\varphi_{j_\kappa}^{(\kappa)}$  for the  $\kappa$ -th DOF ( $1 \leq \kappa \leq f$ ) form a time-dependent orthonormal set. Hence Eq. (1) constitutes an expansion of  $\Psi$  in a time-dependent product basis, formed by products of the SPFs. In turn, the SPFs are expressed in a time-independent “primitive” basis:

**Table 1**  
List of acronyms used frequently in this article.

MCTDH	Multi-Configuration Time-Dependent Hartree
ML-MCTDH	Multi-Layer MCTDH
PES	Potential Energy Surface
MGPF	Multi-Grid Potfit
MCPF	Monte-Carlo Potfit
MLPF	Multi-Layer Potfit
FG-MLPF	Full-Grid Multi-Layer Potfit
RS-MLPF	Random-Sampling Multi-Layer Potfit
SOP	Sum of Products
MLOp	Multi-Layer Operator
SPP	single-particle potential a.k.a. “natural potential”

$$\varphi_j^{(\kappa)}(q_\kappa, t) = \sum_{\alpha=1}^{N_\kappa} A_{j;\alpha}^{(\kappa)}(t) \chi_\alpha^{(\kappa)}(q_\kappa) \quad (2)$$

The primitive basis functions  $\chi_\alpha^{(\kappa)}$  are usually chosen to be the basis functions of a discrete variable representation (DVR) or of other grid-based representations (e.g. FFT), so that  $N_\kappa$  denotes the number of grid points for the  $\kappa$ -th DOF. Note that a direct representation of  $\Psi$  as an expansion in products of primitive basis functions (i.e. the “standard method”) would require  $\prod_{\kappa=1}^f N_\kappa \approx N^f$  coefficients, while the MCTDH representation only requires  $\prod_{\kappa=1}^f n_\kappa \approx n^f$  coefficients for the  $A$ -vector plus  $\sum_{\kappa=1}^f n_\kappa N_\kappa \approx fn$  coefficients for the SPFs, cf. Eq. (2). If  $n \ll N$ , this constitutes a strong reduction of the storage requirements for the wavefunction. This condition can usually be maintained during the time-evolution of  $\Psi$ , at least for some time, because the equations of motion for MCTDH (i.e. how the coefficients  $A$  and  $A^{(\kappa)}$  evolve over time) are derived from the Dirac-Frenkel variational principle [54,55], so that the set of SPFs is variationally optimal for approximating the full  $\Psi$  at each instant.

However, the number of coefficients still scales as  $n^f$ , i.e. exponentially with the number of DOFs. A further reduction can be achieved via “mode combination”, in which several DOFs are combined into one large multi-dimensional mode. Hence the SPFs are not one- but multi-dimensional:

$$\Psi(Q_1, \dots, Q_d, t) = \sum_{j_1=1}^{n_1} \dots \sum_{j_d=1}^{n_d} A_{j_1 \dots j_d}(t) \varphi_{j_1}^{(1)}(Q_1, t) \dots \varphi_{j_d}^{(d)}(Q_d, t) \quad (3)$$

$$\begin{aligned} \varphi_j^{(\kappa)}(Q_\kappa, t) &= \varphi_j^{(\kappa)}(q_{a_\kappa}, \dots, q_{b_\kappa}, t) \\ &= \sum_{\alpha_1=1}^{N_{a_\kappa}} \dots \sum_{\alpha_p=1}^{N_{b_\kappa}} A_{j;\alpha_1 \dots \alpha_p}^{(\kappa)}(t) \chi_{\alpha_1}^{(a_\kappa)}(q_{a_\kappa}) \dots \chi_{\alpha_p}^{(b_\kappa)}(q_{b_\kappa}) \end{aligned} \quad (4)$$

where  $Q_\kappa = (q_{a_\kappa}, \dots, q_{b_\kappa})$  denotes the multi-dimensional coordinate for mode  $\kappa$ . If the set of  $f$  DOFs is combined into  $d$  modes of  $p$  DOFs each (i.e.  $f = pd$ ), and if each mode employs  $n$  SPFs, then the number of coefficients needed to represent  $\Psi$  is  $n^d + dnN^p$ . This achieves another strong reduction in the total number of coefficients.

Taken to the extreme, i.e. combining the DOFs into only few (say,  $d = 2$ ) very large modes, the  $A$ -vector becomes very small ( $\sim n^d$ ) but the SPFs require a large number of coefficients ( $\sim dnN^{f/d}$ ). At this stage it makes sense to introduce another expansion layer, by decomposing the mode  $Q_\kappa$  into a set of  $p_\kappa$  sub-modes,  $Q_\kappa = (Q_{\kappa,1}, \dots, Q_{\kappa,p_\kappa})$ , where each sub-mode  $Q_{\kappa,\lambda}$  is again a set of DOFs. The mode- $\kappa$  SPFs are then expanded in products of sub-mode SPFs, similar to Eq. (1):

$$\begin{aligned} \varphi_j^{(\kappa)}(Q_\kappa, t) &= \varphi_j^{(\kappa)}(Q_{\kappa,1}, \dots, Q_{\kappa,p_\kappa}, t) \\ &= \sum_{k_1=1}^{n_{\kappa,1}} \dots \sum_{k_{p_\kappa}=1}^{n_{\kappa,p_\kappa}} A_{j;k_1 \dots k_{p_\kappa}}^{(\kappa)}(t) \prod_{\lambda=1}^{p_\kappa} \varphi_{k_\lambda}^{(\kappa,\lambda)}(Q_{\kappa,\lambda}, t) \end{aligned} \quad (5)$$

In a two-layer scheme, the sub-mode SPFs  $\varphi^{(\kappa,\lambda)}$  are again expressed in products of primitive basis functions. But one may as well introduce further layers of SPFs, which leads to a hierarchical expansion of  $\Psi$  and gives rise to the multi-layer MCTDH method (ML-MCTDH). The total number of coefficients required to represent  $\Psi$  in ML-MCTDH can be shown, under moderate assumptions, to scale only polynomially instead of exponentially with the number of DOFs (see [24,34] for derivation and discussion). As for the standard MCTDH method, the equations of motion for ML-MCTDH can be derived using the Dirac-Frenkel variational principle.

In the present work, we are interested in computing the ground state of the  $\text{H}_3\text{O}_2^-$  molecule. A simple way to achieve this is by relaxation, i.e. by propagating some initial state  $\Psi_0$  in negative imaginary time  $t = -i\tau$ , for  $\tau \rightarrow \infty$  [56]. This has the effect of exponentially damping all excited state components present in  $\Psi_0$  relative to the ground state component, so that the propagated  $\Psi$  converges to the ground state  $\Psi_{\text{GS}}$  eventually. However, convergence can be slow if there are low-lying excited states. An alternative is the “improved relaxation” method [57,58] where, in turn, the SPFs are relaxed and the  $A$ -vector is obtained by diagonalization. This procedure is iterated until convergence is reached. Not only does the improved relaxation method converge faster to the ground state than regular relaxation, but a block version of the algorithm is additionally able to compute excited states simultaneously. Unfortunately, the Heidelberg MCTDH package [59] currently supports (block) improved relaxation calculations only for MCTDH wavefunctions but not for ML-MCTDH wavefunctions, although it would certainly be possible to do so [60]. In the present work, we therefore resorted to regular relaxation for our ML-MCTDH calculations.

A requirement for an efficient operation of (ML-)MCTDH is that the Hamiltonian must be expressed in a form which allows the efficient evaluation of high-dimensional matrix elements and related quantities, which are encountered during the evaluation of the equations of motion. For example, the expectation value  $\langle \Psi | \hat{H} | \Psi \rangle$  formally constitutes an  $f$ -dimensional integral, but it can be evaluated efficiently if  $\hat{H}$  has a representation as a sum of products (SOP) of one-dimensional operators (here assuming for simplicity that mode combination is not used), i.e.

$$\hat{H} = \sum_{r=1}^s c_r \prod_{\kappa=1}^f \hat{h}_r^{(\kappa)} \quad (6)$$

where the operators  $\hat{h}_r^{(\kappa)}$  operate on the DOF  $q_\kappa$  only. Then the expectation value is evaluated as (cf. Eq. (1))

$$\langle \Psi | \hat{H} | \Psi \rangle = \sum_r c_r \sum_{j_1 \dots j_f} A_{j_1 \dots j_f}^* \sum_{k_1 \dots k_f} A_{k_1 \dots k_f} \prod_{\kappa=1}^f \langle \varphi_{j_\kappa}^{(\kappa)} | \hat{h}_r^{(\kappa)} | \varphi_{k_\kappa}^{(\kappa)} \rangle \quad (7)$$

which boils down to a series of one-dimensional integrals, a sequential series of tensor-matrix products, and a final contraction over  $j_1 \dots j_f$ , all of which can be performed relatively efficiently unless the  $A$ -vector is too large. These steps need to be carried out for each term  $r$  in the SOP expansion, Eq. (6). Hence the computational effort for evaluating Eq. (7), as well as for similar terms appearing in the MCTDH equations of motion, scales linearly with  $s$ , i.e. with the length of the SOP expansion.

The kinetic energy operator (KEO) often naturally has SOP form, at least if a suitable coordinate system is chosen, like polyspherical coordinates [61]. On the other hand, for non-model systems the potential energy operator usually doesn't come in SOP form, but is given by a multi-dimensional potential energy surface (PES) which is obtained as a fit to a large set of electronic structure calculations on a set of judiciously chosen geometries. Such a PES

must be transformed to SOP form before it can be used with MCTDH, as will be discussed in Section 2.2.

For ML-MCTDH, the SOP form can also be evaluated efficiently [24,25]. However, as ML-MCTDH can handle much larger systems (i.e. with more DOFs) than MCTDH, the length of the SOP expansion can become a problematic issue. In Ref. [34], an alternative representation of the Hamiltonian as a “multi-layer operator” (MLOp) was developed, which possesses the same compact hierarchical structure as the ML-MCTDH wavefunction. It was demonstrated that this structure can lead to a much more efficient evaluation of the terms in the ML-MCTDH equations of motion, already for systems as small as  $f = 4$ , and with potentially vast computational savings for large systems. As for the SOP form, a way to transform general PES into MLOp form is needed, which will likewise be discussed in Section 2.2.

## 2.2. Variational grid-based PES fitting methods

One popular method for transforming a PES  $V(q_1, \dots, q_f)$  into SOP form is the Potfit algorithm [49]. This grid-based method starts by evaluating the PES on a product grid of points  $(q_{\alpha_\kappa}^{(\kappa)}, \kappa = 1 \dots f)$ , which yields an  $f$ -dimensional tensor

$$V_{\alpha_1 \dots \alpha_f} = V(q_{\alpha_1}^{(1)}, \dots, q_{\alpha_f}^{(f)}); \quad 1 \leq \alpha_\kappa \leq N_\kappa \quad (8)$$

Similar to the MCTDH ansatz Eq. (1), this tensor is then approximated by expanding it in a basis of “single-particle potentials” (SPPs)

$$V_{\alpha_1 \dots \alpha_f} \approx \tilde{V}_{\alpha_1 \dots \alpha_f} = \sum_{j_1=1}^{m_1} \dots \sum_{j_f=1}^{m_f} C_{j_1 \dots j_f} v_{\alpha_1 j_1}^{(1)} \dots v_{\alpha_f j_f}^{(f)} \quad (9)$$

where the  $v_{\alpha_\kappa j_\kappa}^{(\kappa)}$  are the components of the SPPs for DOF  $\kappa$ ,  $C$  is an  $f$ -dimensional coefficient tensor (the “core tensor”), and the  $m_\kappa$  are expansion orders. Eq. (9) is also known as a (truncated) Tucker decomposition [50].

To obtain the SPPs, Potfit builds a “potential density matrix”  $\rho^{(\kappa)} \in \mathbb{R}^{N_\kappa \times N_\kappa}$  for each DOF  $\kappa$  by contracting the tensor  $V$  with itself over all DOFs except the  $\kappa$ -th one, i.e.

$$\rho_{\alpha\beta}^{(\kappa)} = \sum_{\alpha_1=1}^{N_1} \dots \sum_{\alpha_{\kappa-1}=1}^{N_{\kappa-1}} \sum_{\alpha_{\kappa+1}=1}^{N_{\kappa+1}} \dots \sum_{\alpha_f=1}^{N_f} V_{\alpha_1 \dots \alpha_{\kappa-1} \alpha \alpha_{\kappa+1} \dots \alpha_f} V_{\alpha_1 \dots \alpha_{\kappa-1} \beta \alpha_{\kappa+1} \dots \alpha_f} \quad (10)$$

These density matrices are then diagonalized to obtain eigenvalues  $\lambda_j^{(\kappa)}$  (the “natural weights”) and eigenvectors  $v_j^{(\kappa)}$  (the “natural potentials”),  $1 \leq j \leq N_\kappa$ . Only the dominant  $m_\kappa$  natural potentials (i.e. those corresponding to the largest natural weights) are kept as the SPPs. Finally, the core tensor  $C$  is found by projecting the tensor  $V$  onto products of the SPPs. A mathematically equivalent algorithm is known as the higher-order singular value decomposition (HOSVD) [62].

Except for  $f = 2$ , Potfit does not yield the optimal SPPs and core tensor. However, the error  $\Delta = \|V - \tilde{V}\|$  introduced by Potfit can be bounded by the sum of the neglected natural weights [51],

$$\frac{1}{f-1} \sum_{\kappa=1}^f \sum_{j>m_\kappa} \lambda_j^{(\kappa)} \leq \Delta_{\text{opt}}^2 \leq \Delta^2 \leq \sum_{\kappa=1}^f \sum_{j>m_\kappa} \lambda_j^{(\kappa)} \quad (11)$$

where  $\Delta_{\text{opt}}$  is the best possible approximation of  $V$  in the form Eq. (9) with fixed expansion orders  $m_\kappa$ . This shows that the Potfit approximation is at most a factor of  $\sqrt{f-1}$  worse than the best possible approximation of the same form and size. It also shows that in order to significantly increase the accuracy of the approximation, it will be necessary to increase the expansion orders  $m_\kappa$ , as this is the only way to reduce the lower bound in Eq. (11).

The number of SOP terms generated by the Potfit expansion according to Eq. (9) is the number of entries in the core tensor,  $\sim m^f$ . This can be reduced by a factor of  $m$  by contracting the core tensor with the SPPs of one DOF (the “contracted mode”), e.g. the first one:

$$D_{\alpha_1 j_2 \dots j_f}^{(1)} = \sum_{j_1=1}^{m_1} C_{j_1 \dots j_f} v_{\alpha_1 j_1}^{(1)} \quad (12)$$

$$\tilde{V}_{\alpha_1 \dots \alpha_f} = \sum_{j_2=1}^{m_2} \dots \sum_{j_f=1}^{m_f} D_{\alpha_1 j_2 \dots j_f}^{(1)} v_{\alpha_2 j_2}^{(2)} \dots v_{\alpha_f j_f}^{(f)} \quad (13)$$

In doing so, one may as well choose  $m_1 = N_1$  in order to reduce the Potfit error. The resulting expansion, Eq. (13), thus generates  $\sim m^{f-1}$  SOP terms.

A major disadvantage of Potfit is that it needs to build the PES tensor  $V$  on the full product grid, which has  $\sim N^f$  entries. In practice this limits the applicability of Potfit to systems with 6–8 DOFs, otherwise the computation of all the entries of  $V$  and of the potential density matrices becomes too expensive. Recently, two methods have been proposed for overcoming this limitation of Potfit, i.e. they avoid running over the full product grid. Reviewing Eq. (10), we note that the potential density matrices for DOF  $\kappa$  are computed by integrating over the *complementary* grid, i.e. the product grid of all DOFs except the  $\kappa$ -th. Instead of performing this  $(f-1)$ -dimensional integration exactly, one can perform it approximately. In *Monte-Carlo Potfit* (MCPF) [52], the integration over the complementary grid is replaced by a Monte-Carlo integration, i.e. by sampling the grid points for integration either uniformly from the full grid or via the Metropolis–Hastings algorithm [63,64]. Additional steps are then required for computing the core tensor, to correct for the error introduced by approximating the integration over the complementary grid. In *multigrid Potfit* (MGPF) [51], in addition to the original full “fine” product grid, a “coarse” product grid is introduced, which consists of a subset of the fine grid points. In between these two limiting cases one then defines a series of partial grids where one mode lies on the fine grid and the rest lie on the coarse grid. The SPPs on the fine grid are obtained through an interpolation process in which SPPs from a coarse-grid Potfit are transferred onto the fine grid by multiplication with a product of approximated density matrices computed on the partial grids. For details of both MGPF and MCPF the reader is referred to the original publications [51,52].

Another problem of Potfit is that the resulting number of SOP terms ( $\sim m^{f-1}$ , cf. Eq. (13)) grows exponentially with the number  $f$  of DOFs. This problem is not overcome by MGPF or MCPF, as they “only” provide more efficient methods to compute a representation in SOP form, but cannot overcome the fundamental limitation given by the Potfit error estimate, Eq. (11). Especially if a high accuracy of the PES representation is needed, it is necessary to increase the expansion orders  $m_\kappa$ , so that the number of terms in the Potfit expansion quickly becomes prohibitive due to its exponential scaling. In the context of ML-MCTDH, this fundamental problem can be overcome by abandoning the SOP form and switching to the hierarchical MLOp form for representing the PES. Again, this poses the problem of how to transform a general PES into MLOp form, and the *multi-layer Potfit* (MLPF) method [34] has been developed for this purpose, based on the hierarchical singular value decomposition [53]. In Ref. [34], MLPF was applied to a relatively small system (diatom-diatom scattering) and the PESs which had to be transformed were 5-dimensional. Despite the small dimensionality, MLPF achieved a strong reduction of the computational resources required for the ML-MCTDH propagations (both in CPU and RAM), compared to using Potfit at the same accuracy.

As originally conceived, MLPF suffers from the same problem as Potfit, in that it requires running over the full product grid in order to transform the PES into MLOp form, which again limits applicability to 6–8 DOFs. In the present article, we will explore two options for overcoming this limitation. The first option makes use of the fact that the first step of MLPF is identical to Potfit, except that contraction is not used. Hence one may use MGPF or MCPF to compute an initial Potfit, undo the contraction<sup>1</sup> to obtain SPPs for the contracted mode as well as the core tensor  $C$  (cf. Eq. (9)), and then perform the remaining steps of MLPF. These steps are computationally cheap compared to the initial Potfit, as they don't need to operate on the full-grid PES but only on the  $C$  tensor which is much smaller. MLPF reshapes the  $C$  tensor by combining low-dimensional modes into higher-dimensional modes and performs another HOSVD step in order to reduce its data, and repeats this process until only a few (usually 2 or 3) large-dimensional modes are left. In contrast to performing MLPF on the full-grid PES, this way of using MLPF as a postprocessing option to MGPF/MCPF fully avoids the full-grid problem, and is rather fast and simple to perform. However, the accuracy of this approach can be limited, because in a high-accuracy setting the initial Potfit produced by MGPF/MCPF might become very large due to its inherent scaling behavior.

The second option is to integrate the approximation ideas from MGPF or MCPF directly into MLPF. The goal is to avoid the explicit computation of the core tensor, which easily becomes the bottleneck if high accuracy (i.e. large expansion orders  $m_\kappa$ ) are required. As a first step in this direction, in Section 2.3 we will present a variant of MLPF which avoids running over the full product grid by using uniform random sampling as in MCPF, while also avoiding to compute the core tensor as an intermediate step. As we will show, this new variant of MLPF is able to produce rather accurate PES fits in MLOp form with modest computational resources, however its implementation currently only has prototype status so that it may not be readily applicable for systems with a different number of modes or a different multi-layer structure than investigated here. To make the distinction between the new variant and the original MLPF method more clear, we will henceforth refer to the original method as “full-grid MLPF” (FG-MLPF).

### 2.3. Random Sampling Multi-Layer Potfit (RS-MLPF)

In order to avoid an overly technical exposition, here we present the RS-MLPF algorithm for a balanced binary multi-layer tree with eight uncombined primitive modes, i.e. a three-layer tree. The generalization to arbitrary tree structures is relatively straightforward, but would require an overabundance of additional notation. In the following,  $\kappa = 1 \dots 8$  numbers the DOFs,  $N_\kappa$  denotes the number of grid points for the  $\kappa$ -th DOF, and  $\alpha_\kappa = 1 \dots N_\kappa$  indexes these grid points.

In the first step, RS-MLPF proceeds like Monte Carlo Potfit [52]. The potential density matrix for the 1st DOF is defined as

$$\rho_{\alpha_1 \alpha'_1}^{(1)} = \sum_{\alpha_2 \dots \alpha_8} V_{\alpha_1 \alpha_2 \dots \alpha_8} V_{\alpha'_1 \alpha_2 \dots \alpha_8} \quad (14)$$

where  $V$  denotes the eight-dimensional PES tensor defined on the full grid. This 7D integration is then replaced by a Monte Carlo integration, using  $R$  sampling points  $\{(\alpha_2^r \dots \alpha_8^r) | r = 1 \dots R\}$ :

$$\rho_{\alpha_1 \alpha'_1}^{(1)} = \sum_r V_{\alpha_1 \alpha_2^r \dots \alpha_8^r} V_{\alpha'_1 \alpha_2^r \dots \alpha_8^r} \quad (15)$$

To avoid a rank-deficient  $\rho^{(1)}$ , one should choose  $R > N_1$ . In practice, we choose  $R = qN_1$ , where  $q$  is the *oversampling parameter*. A larger  $q$  will result in using more sampling points, and thus

<sup>1</sup> The potential density matrix for the contracted mode can be computed (approximately) by self-contracting the  $D$ -tensor, cf. Eq. (12), to form  $\rho_{\alpha\beta}^{(1)}$ .

in a more accurate estimation of the potential density matrices. Despite the Monte Carlo approximation,  $\rho^{(1)}$  is symmetric and positive semi-definite. Diagonalizing  $\rho^{(1)}$  yields natural weights and natural potentials, of which only the dominant  $m_1$  ones are kept. Mathematically equivalent, we reshape the sampled  $V$  tensor into a matrix  $V^{(1)}$  with entries  $V_{\alpha_1 r}^{(1)} = V_{\alpha_1 \alpha_2^r \dots \alpha_8^r}$ , and perform a singular value decomposition (SVD) on this matrix. Its left singular vectors then yield the natural potentials, and the squares of the singular values yield the natural weights. Numerically this approach is more stable, hence it is the choice used in practice. Using the same procedure for the other DOFs, we obtain all natural potentials for the lowest (third, in our example) layer:

$$u_{\alpha_\kappa i_\kappa}^{(\kappa)}; \quad \kappa = 1 \dots 8, \quad \alpha_\kappa = 1 \dots N_\kappa, \quad i_\kappa = 1 \dots m_\kappa \quad (16)$$

The core tensor for these natural potentials is

$$C_{i_1 \dots i_8} = \sum_{\alpha_1 \dots \alpha_8} u_{\alpha_1 i_1}^{(1)} \dots u_{\alpha_8 i_8}^{(8)} V_{\alpha_1 \dots \alpha_8} \quad (17)$$

but we can actually avoid computing it, because in MLPF  $C$  is only needed to compute the density matrices for the next higher layer. Introducing the mode-combined indices

$$b_1 = (i_1 i_2) \quad b_2 = (i_3 i_4) \quad b_3 = (i_5 i_6) \quad b_4 = (i_7 i_8), \quad (18)$$

the density matrix for mode 1 in the second layer (which comprises DOFs 1 and 2) reads

$$\bar{\rho}_{b_1 b'_1}^{(1)} = \sum_{b_2 b_3 b_4} C_{b_1 b_2 b_3 b_4} C_{b'_1 b_2 b_3 b_4} \quad (19)$$

We can now formally insert the expression for  $C$ , Eq. (17), and for the purpose of this computation we can furthermore choose full expansion orders  $m_3 = N_3, \dots, m_8 = N_8$  which makes the natural potential bases for DOFs 3 through 8 complete. Using this completeness property, we find that  $\bar{\rho}^{(1)}$  can be computed via

$$\bar{\rho}_{b_1 b'_1}^{(1)} = \sum_{\alpha_3 \dots \alpha_8} D_{b_1 \alpha_3 \dots \alpha_8}^{(1)} D_{b'_1 \alpha_3 \dots \alpha_8}^{(1)} \quad (20)$$

$$D_{b_1 \alpha_3 \dots \alpha_8}^{(1)} = \sum_{\alpha_1 \alpha_2} u_{\alpha_1 i_1}^{(1)} u_{\alpha_2 i_2}^{(2)} V_{\alpha_1 \dots \alpha_8} \quad (21)$$

Here,  $\bar{\rho}^{(1)}$  is computed via a 6D integration, which we again replace by a Monte Carlo integration, using a new set of  $\bar{R}$  sampling points  $\{A^r := (\alpha_3^r \dots \alpha_8^r) | r = 1 \dots \bar{R}\}$ :

$$\bar{\rho}_{b_1 b'_1}^{(1)} = \sum_r D_{b_1 \alpha_3^r \dots \alpha_8^r}^{(1)} D_{b'_1 \alpha_3^r \dots \alpha_8^r}^{(1)}. \quad (22)$$

Again, to avoid rank deficiency one should choose  $\bar{R} > m_1 m_2$  and in practice we use  $\bar{R} = qm_1 m_2$ . From expression (22) it becomes clear that  $D_{bA}^{(1)}$  doesn't need to be known on the full product grid, but only on the sampling points  $\{A^r\}$ . It now remains to evaluate  $D_{bA}^{(1)}$  for these points. In principle, this could be achieved by directly evaluating Eq. (21), but this may become too costly for large modes. Alternatively, we note that the PES approximation is now given by

$$\tilde{V}_{\alpha_1 \dots \alpha_8} = \sum_{i_1 i_2} D_{i_1 i_2 \alpha_3 \dots \alpha_8}^{(1)} u_{i_1 \alpha_1}^{(1)} u_{i_2 \alpha_2}^{(2)} \quad (23)$$

and that the optimal approximation is achieved by minimizing  $\|V - \tilde{V}\|^2$  w.r.t.  $D_{bA}^{(1)}$ . This leads to the equation

$$\sum_{\alpha_1 \alpha_2} \Omega_{\alpha_1 \alpha_2, b}^{(1)} V_{\alpha_1 \alpha_2 A} = \sum_{b'} \left( \sum_{\alpha_1 \alpha_2} \Omega_{\alpha_1 \alpha_2, b}^{(1)} \Omega_{\alpha_1 \alpha_2, b'}^{(1)} \right) D_{b' A}^{(1)} \quad (24)$$

$$\text{where } \Omega_{\alpha_1 \alpha_2, b}^{(1)} = u_{\alpha_1 i_1}^{(1)} u_{\alpha_2 i_2}^{(2)} \quad (25)$$

If the summation over  $\alpha_1 \alpha_2$  is carried out fully, then the term in parentheses yields  $\delta_{bb'}$  (due to orthonormality of the natural potentials) and one arrives back at Eq. (21). Instead we can replace this sum (both on the LHS and on the RHS) by a Monte Carlo integration. Using the new set of  $\bar{S}$  sampling points  $\{(\alpha_1^s \alpha_2^s) | s = 1 \dots \bar{S}\}$ , this results in

$$D_{bA}^{(1)} = \sum_{b'} (X^{(1)})_{bb'}^{-1} \sum_s \Omega_{\alpha_1^s \alpha_2^s, b}^{(1)} V_{\alpha_1^s \alpha_2^s A} \quad (26)$$

$$\text{where } X_{bb'}^{(1)} = \sum_s \Omega_{\alpha_1^s \alpha_2^s, b}^{(1)} \Omega_{\alpha_1^s \alpha_2^s, b'}^{(1)} \quad (27)$$

Here we must choose  $\bar{S} > m_1 m_2$ , otherwise the matrix  $X^{(1)}$  won't be invertible. Again, our choice in practice is  $\bar{S} = q m_1 m_2$ . Once  $D_{bA}^{(1)}$  is computed, the density matrix  $\bar{\rho}^{(1)}$  is easily computed via Eq. (22) and diagonalized (or mathematically equivalent, an SVD of the matrix  $D_{bA}^{(1)}$  is performed, similar to the previous layer). Doing so for all four modes of layer 2 yields their natural potentials, and again, only the dominant ones are kept:

$$\bar{u}_{b_{\kappa j_{\kappa}}}^{(\kappa)}; \quad \kappa = 1 \dots 4, \quad b_{\kappa} = 1 \dots m^2, \quad j_{\kappa} = 1 \dots \bar{m}_{\kappa} \quad (28)$$

Thus we have achieved the computation of the natural potentials for layer 2, while avoiding to compute the intermediate core tensor  $C$ .

If we stopped the expansion at layer 2, we would need to use the core tensor

$$\bar{C}_{j_1 \dots j_4} = \sum_{b_1 \dots b_4} \bar{u}_{b_1 j_1}^{(1)} \dots \bar{u}_{b_4 j_4}^{(4)} C_{b_1 \dots b_4} \quad (29)$$

Considering that we don't actually know  $C$ , we again aim to avoid this computation. To this end we formally insert the definition of  $C$ , Eq. (17), into Eq. (29):

$$\begin{aligned} \bar{C}_{j_1 \dots j_4} &= \sum_{i_1 \dots i_8} \bar{u}_{i_1 j_1}^{(1)} \dots \bar{u}_{i_4 j_4}^{(4)} \sum_{\alpha_1 \dots \alpha_8} u_{\alpha_1 i_1}^{(1)} u_{\alpha_2 i_2}^{(2)} \dots u_{\alpha_7 i_7}^{(7)} u_{\alpha_8 i_8}^{(8)} V_{\alpha_1 \dots \alpha_8} \\ &= \sum_{\alpha_1 \dots \alpha_8} \left[ \sum_{i_1 i_2} u_{\alpha_1 i_1}^{(1)} u_{\alpha_2 i_2}^{(2)} \bar{u}_{i_1 i_2 j_1}^{(1)} \right] \times \dots \times \left[ \sum_{i_7 i_8} u_{\alpha_7 i_7}^{(7)} u_{\alpha_8 i_8}^{(8)} \bar{u}_{i_7 i_8 j_4}^{(4)} \right] V_{\alpha_1 \dots \alpha_8} \\ &= \sum_{\alpha_1 \dots \alpha_8} \bar{u}_{\alpha_1 \alpha_2 j_1}^{(1)} \dots \bar{u}_{\alpha_7 \alpha_8 j_4}^{(4)} V_{\alpha_1 \dots \alpha_8} \end{aligned} \quad (30)$$

where we have introduced the abbreviations

$$\bar{u}_{\alpha_1 \alpha_2 j_1}^{(1)} = \sum_{i_1 i_2} u_{\alpha_1 i_1}^{(1)} u_{\alpha_2 i_2}^{(2)} \bar{u}_{i_1 i_2 j_1}^{(1)} \quad (31)$$

etc. At this level, the approximation for the PES tensor  $V$  reads

$$\bar{V}_{\alpha_1 \dots \alpha_8} = \sum_{j_1 \dots j_4} \bar{C}_{j_1 \dots j_4} \bar{u}_{\alpha_1 \alpha_2 j_1}^{(1)} \dots \bar{u}_{\alpha_7 \alpha_8 j_4}^{(4)} \quad (32)$$

and as for the previous layer, the optimal  $\bar{C}$  is obtained from minimizing  $\|V - \bar{V}\|^2$  w.r.t.  $\bar{C}_J$ , where we have introduced the multi-index  $J = (j_1 \dots j_4)$ . This eventually leads to the equation

$$\bar{C}_J = \sum_{J'} (\bar{X}^{(-1)})_{JJ'} \sum_A \bar{\Omega}_{AJ'} V_A \quad (33)$$

$$\text{where } \bar{X}_{JJ'} = \sum_A \bar{\Omega}_{AJ} \bar{\Omega}_{AJ'} \quad (34)$$

$$\text{and } \bar{\Omega}_{AJ} = \bar{u}_{\alpha_1 \alpha_2 j_1}^{(1)} \dots \bar{u}_{\alpha_7 \alpha_8 j_4}^{(4)} \quad (35)$$

and  $A = (\alpha_1 \dots \alpha_8)$  is a full-grid multi-index. As before, the summations over  $A$  are replaced by Monte Carlo integrations, but to avoid dealing with a very large  $\bar{\Omega}$  matrix, we choose a set of sampling points separately for the first four and the last four DOFS, i.e. we use the point set  $\{A^{rs} = (\alpha_1^r \dots \alpha_4^r \alpha_5^s \dots \alpha_8^s) | r = 1 \dots \bar{R}, s = 1 \dots \bar{S}\}$ . This results in a separable structure of the matrices  $\bar{\Omega}$  and  $\bar{X}$  which

greatly reduces the computational effort for the linear algebra parts of Eqs. (33)–(35) but requires more PES evaluations. To ensure invertibility of  $\bar{X}$ , we must choose  $\bar{R} > \bar{m}_1 \bar{m}_2$  and  $\bar{S} > \bar{m}_3 \bar{m}_4$ . Starting with the already known natural potentials for layers 3 and 2, we can evaluate Eqs. (31), (35), (34), and (33) in sequence to obtain  $\bar{C}$ .

Finally, we introduce a next layer of mode-combined indices

$$c_1 = (j_1 j_2) \quad c_2 = (j_3 j_4) \quad (36)$$

and rewrite the tensor  $\bar{C}_{j_1 j_2 j_3 j_4}$  as a matrix  $\bar{C}_{c_1 c_2}$ , on which we perform a singular value decomposition:

$$\bar{C}_{c_1 c_2} = \sum_{k_1 k_2} \bar{C}_{k_1 k_2} \bar{u}_{c_1 k_1}^{(1)} \bar{u}_{c_2 k_2}^{(2)} \quad (37)$$

where the top-level (L1) core tensor  $\bar{C}$  is diagonal. The left ( $\bar{u}^{(1)}$ ) and right ( $\bar{u}^{(2)}$ ) singular vectors serve as the natural potentials for the two L1 modes, and we only keep the  $\bar{m}$  dominant ones. This completes the RS-MLPF algorithm, as we have now obtained the natural potentials for all modes of all layers as well as the top-level core tensor.

For the purposes of this study, we have created a prototype implementation of the RS-MLPF algorithm in the high-level programming language Julia [65]. Our implementation is currently restricted to a balanced binary tree with two or three layers (i.e. 4 or 8 primitive modes). Moreover, all Monte Carlo integrations are simply done by uniform random sampling over all grid points. Like for the FG-MLPF algorithm described in [34], the algorithm automatically determines all the expansion orders  $m_1 \dots m_8, \bar{m}_1 \dots \bar{m}_4$ , and  $\bar{m}$  by taking a user-prescribed threshold for the global RMS error and distributing it evenly over all modes in the multi-layer tree. However, the errors introduced by the various Monte Carlo integrations are not taken into account in this error control scheme, so that the actual fit error is larger than for FG-MLPF. This additional random sampling error ("RS error") can be reduced by increasing the oversampling parameter  $q$ . We point out that our RS-MLPF implementation is not yet optimized nor parallelized, but as we will show in Section 4, it already enables us to obtain highly accurate PES fits with rather modest computational resources.

### 3. The $\text{H}_3\text{O}_2^-$ ion

The  $\text{H}_3\text{O}_2^-$  ion is an interesting prototype for understanding the anomalous high mobility of the hydroxide ion in water [66–70]. Electronic structure calculations reveal that at its energetic minimum,  $\text{H}_3\text{O}_2^-$  possess a slightly asymmetric structure, where the bridging hydrogen is closer to one oxygen than to the other [68]. However, quantum dynamical calculations show that the bridging hydrogen is well shared between the two OH moieties, as there is a very low barrier ( $\sim 70 \text{ cm}^{-1}$ ) for the proton transfer [71].

Our (ML-)MCTDH calculations make use of the PES3C potential energy surface [68,71], which was constructed as a least-squares fit to  $\sim 23,000$  energy points calculated at the CCSD(T) level with an aug-cc-pVTZ basis set. This PES is a more global variant of its predecessor PES2 [68], as it includes a number of dissociative conformations. The fit sports a relatively low root-mean-square (RMS) error of 18.0 and  $103 \text{ cm}^{-1}$  for energies up to 6,000 and  $30,000 \text{ cm}^{-1}$ , respectively. An important feature of the PES3C surface is its permutational invariance, i.e. the PES value is invariant under interchange of like atoms (H with H, or O with O).

Even in its ground state, the  $\text{H}_3\text{O}_2^-$  ion is affected by large-amplitude motions and strong anharmonicity, as the PES features two shallow double-well potentials: one along the proton-transfer coordinate (with a barrier of  $74 \text{ cm}^{-1}$  according to PES3C), and another along the torsional coordinate around the O-O axis

(barriers of 374 cm<sup>-1</sup> and 147 cm<sup>-1</sup> at 0° and 180°, respectively). These features lead to strong correlations between the DOFs, which justify the need for full-dimensional quantum calculations to investigate this system.

The PES3C surface has been previously used to compute the ground state (zero-point) energy of H<sub>3</sub>O<sub>2</sub><sup>-</sup> as well as vibrationally excited states. McCoy et al. [71] report results from vibrational configuration-interaction (VCI) and diffusion Monte-Carlo (DMC) calculations, yielding ground state (GS) energies of 6625 cm<sup>-1</sup> (VCI) and 6605 ± 5 cm<sup>-1</sup> (DMC), respectively. However, these reported values were obtained with the PES2 surface, though further calculations with the PES3C surface differed by less than 5 cm<sup>-1</sup> [71] for the DMC results. Additional results for the PES3C surface were obtained by Yu [70] who used a two-layer Lanczos algorithm with mixed grid/non-direct product basis set and reported a GS energy of 6623.5 cm<sup>-1</sup>. More recently, in a series of papers [51,21,22] Peláez et al. investigated ground and excited states of H<sub>3</sub>O<sub>2</sub><sup>-</sup> with the MCTDH method, where improved relaxation was used to obtain the states and MGPF was used to transform the PES3C surface into SOP form. For the most accurate PES fit, the reported GS energy was 6602 cm<sup>-1</sup>.

In this work we use the same valence coordinate system as in the previous works of Peláez et al. [21,22]. (cf. Fig. 1). This coordinate system is defined by two vectors  $\mathbf{r}_1$  and  $\mathbf{r}_2$  for the two O-H moieties, a vector  $\mathbf{R}$  connecting the O atoms, and a vector  $\mathbf{r}_3 = (x, y, z)$  connecting the center of the O-O vector  $\mathbf{R}$  to the bridging H atom. Ignoring the overall rotation, this yields nine coordinates for describing the system: the O-H bond lengths  $r_1$  and  $r_2$ , the O-O distance  $R$ , the position of the bridging H  $(x, y, z)$ , the azimuthal angles  $\theta_1$  and  $\theta_2$  between the O-H vectors and the O-O axis (though note that the calculations actually use  $u_i = \cos \theta_i$ , cf. Table 2), and the torsional angle  $\phi$ . As suggested by Vendrell et al. [17], we replace the coordinate  $z$  by a dimensionless variable  $z_{\text{red}} = z/(R - 2d_0)$  which can take values in the range  $[-0.5, 0.5]$ .  $d_0$  is a parameter which signifies the minimum allowed distance of the bridging H to one of the O atoms. Here we use  $d_0 = 1.6a_0$ . In this way, highly energetic conformations in which the bridging H lies too close to one of the O atoms are avoided.

As noted by Yu [70] and Peláez et al. [51], the PES3C energy surface exhibits “holes”, i.e. unphysical regions where the potential energy lies below the (physically sound) global potential minimum. As such regions pose problems both for the PES fitting (where they introduce artificial correlations between the DOFs) and for the quantum calculations (where they may act as a trap for the wavefunction), it is advisable to repair or avoid those regions. While Yu [70] replaced all negative energies with a large positive value<sup>2</sup> so that the wavefunction avoids the unphysical regions, Peláez et al. [51,21] carefully reduced the coordinate ranges so that no regions of negative energy can be encountered. However, unphysically distorted PES regions could not be excluded to be present in the grid, which might lead to unphysical correlation between the DOFs. Here we follow Peláez’ approach, and reuse the coordinate ranges as well as other parameters defining the primitive grid from the previous works [21,22]. These parameters are listed in Table 2.

## 4. Results

Using four different variants of Potfit, we have computed the ground state (GS) of the H<sub>3</sub>O<sub>2</sub><sup>-</sup> ion, for which the PES3C potential energy surface described in Section 3 was used. Our investigation focuses on how the accuracy of the PES fit influences the runtime of the GS computation.

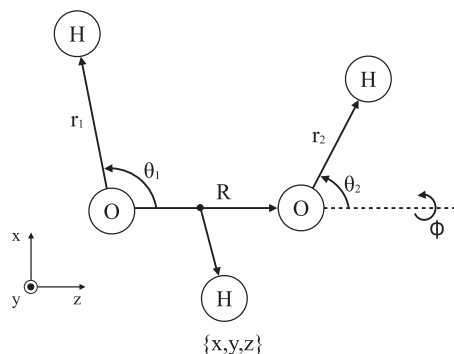


Fig. 1. Valence coordinates for H<sub>3</sub>O<sub>2</sub><sup>-</sup>.

Table 2

Definition of the primitive grid. The DVR column indicates the type of the discrete variable representation used for each DOF: harmonic oscillator (HO), sine (sin), or exponential (exp) DVR.  $N$  is the number of grid points for each DOF. Instead of the angles  $\theta_i$  we use the variables  $u_i = \cos \theta_i$ . All distance coordinates ( $r_1, r_2, R, x, y$ ) are measured in bohr, and  $\phi$  in radians.  $u_1, u_2$ , and  $z_{\text{red}} = z/(R - 2d_0)$  (see text) are dimensionless.

DOF	DVR	$N$	Range
$r_1$	HO	13	[1.4, 2.4]
$r_2$	HO	13	[1.4, 2.4]
$R$	HO	11	[4.15, 5.5]
$x$	HO	10	[-0.8, 0.8]
$y$	HO	10	[-0.8, 0.8]
$z_{\text{red}}$	HO	20	[-0.5, 0.5]
$u_1$	sin	12	[-0.8, 0.35]
$u_2$	sin	12	[-0.35, 0.8]
$\phi$	exp	21	[0, 2 $\pi$ )

### 4.1. Computational setup

To discretize the system, we employed the same primitive basis as in Ref. [21], and the basis parameters are listed in Table 2. We also reuse the kinetic energy operator from [21] which was derived as an analytic expression using the TANA software package [72]. However, we used a different mode combination setup than in [21] because here we perform most computations with ML-MCTDH instead of MCTDH, and we found that the original mode combination scheme led to suboptimal performance of ML-MCTDH, and that a different scheme yielded an improved balance of the ML-MCTDH tree. The primitive combined modes we used for our MCTDH calculations are:  $(r_1, u_1), (R, z_{\text{red}}), (x, y, \phi)$ , and  $(r_2, u_2)$ . For our ML-MCTDH calculations, the first two and the last two of these primitive modes were then combined for the upper layer. The resulting ML-MCTDH tree is depicted in Fig. 2.

In addition to this setup with four modes, we have performed a set of ML-MCTDH computations with eight modes, where all primitive modes contain only one DOF except for the combined mode  $(x, y)$ . The resulting ML-MCTDH tree is shown in Fig. 3. We note that, at the desired level of accuracy for the wavefunction, MCTDH computations with eight modes would be much too costly. Therefore all 8-mode computations were carried out with ML-MCTDH.

To obtain the system’s ground state, we used the improved relaxation method with MCTDH as well as regular relaxation (i.e. propagation in negative imaginary time) with ML-MCTDH. All computations started with the same initial wavefunction, which was defined as a Hartree product of Gaussians around the energy-optimized geometry. In order to quickly obtain a state relatively close to the ground state, we first performed a set of short relaxation runs, using gradually increasing number of SPFs and increasing integrator accuracy. The state obtained in this initial

<sup>2</sup> We note that this procedure might shift the GS energy upwards.



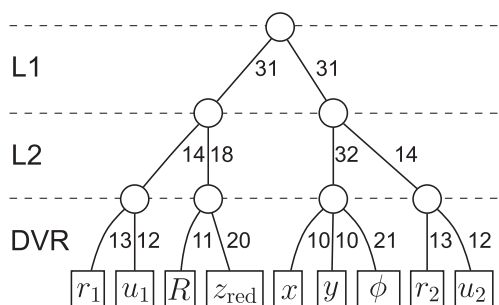


**Fig. 2.** ML-MCTDH wavefunction tree used for our 4-mode computations. The edges are labeled with the number of basis functions for each mode, i.e. the number of DVR grid points for the primitive modes (bottom), and the number of SPFs for layer 2 (L2) and layer 1 (L1) modes.

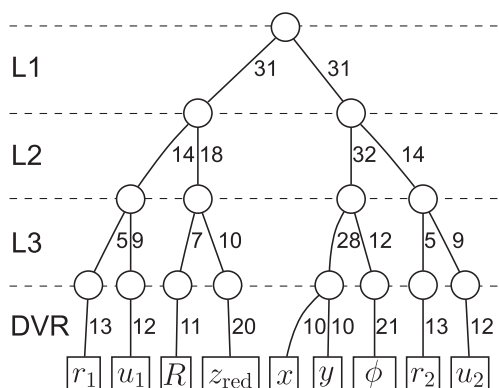


**Fig. 3.** ML-MCTDH wavefunction tree used for our 8-mode computations. The edges are labeled as in Fig. 2, and a third layer of SPFs (L3) has been added.

phase was then subjected to a long relaxation run (nominal propagation time 1000 fs), using high integrator accuracy and the number of SPFs as indicated in Figs. 2 and 3. We note that with these settings, the lowest natural populations for all modes never exceeded  $10^{-7}$ , which shows that our wavefunction representation is highly accurate. Finally, to check that the GS energy is converged, the number of SPFs for all modes was slightly increased, and a further short relaxation run was performed. In all our computations, the energy dropped at most by  $0.01 \text{ cm}^{-1}$ , which indicates that convergence had been achieved. All relaxation runtimes reported below refer to the long main relaxation run over 1000 fs, as this was the part which dominated the runtime of the ground state computation.

For MCTDH, we used the same number of SPFs as for L2 of the ML-MCTDH tree, i.e. 14/18/32/14, resulting in an  $A$ -vector of 112,896 elements. As discussed in Section 2.1, the improved relaxation method only uses propagation for the SPFs but diagonalization to obtain the  $A$ -vector. Nevertheless, we found that the convergence behaviour towards the GS differs very little between improved relaxation runs and regular relaxation runs, as demonstrated by the relaxation profiles shown in Fig. 4. Note that both methods indeed need about 1000 fs to converge to the GS. This allows us to make a fair comparison between the runtimes for these two relaxation calculations, despite their algorithmic differences.

#### 4.2. PES fits

We have produced a series of fits of the PES3C surface, using four different variants of Potfit:

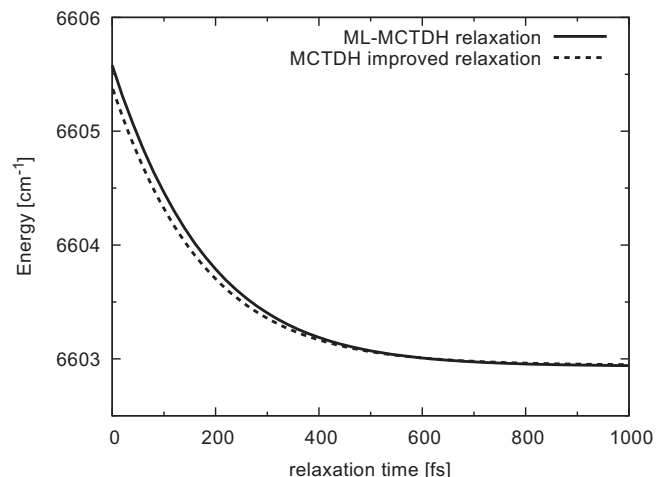


**Fig. 4.** Evolution of the energy expectation value  $\langle \Psi | \hat{H} | \Psi \rangle$  over the course of the relaxation, for one exemplary MCTDH improved relaxation calculation and one exemplary ML-MCTDH relaxation calculation.

- MGPF.** We used multi-grid Potfit (MGPF) in its top-down variant, in which a very large coarse grid is chosen, essentially utilizing every second fine grid point. This produced a fit of very high accuracy with 49, 338, and 49 SPPs for the modes  $(r_1, u_1)$ ,  $(x, y, \phi)$ , and  $(r_2, u_2)$ , respectively. As in [21], the mode  $(R, z_{\text{red}})$  was contracted. This fit itself would be too large to perform MCTDH calculations, but it can be used as a starting point for creating more reasonably sized fits by truncating the number of SPPs for each mode, based on a threshold for their natural weights. We thus produced three fits at different levels of accuracy, which we refer to by their relative quality: low (using 14/22/14 SPPs), medium (18/38/18), and high (23/56/23). The resulting fits in SOP form are suitable for both MCTDH and ML-MCTDH calculations.
- MGPF + MLPF.** Each of the three MGPF fits was then post-processed by MLPF, namely the first step of FG-MLPF can be replaced by reading in the SOP fit produced by MGPF, computing the SPPs for the contracted mode, and then the remaining steps of FG-MLPF are completed. The FG-MLPF implementation can automatically determine the expansion orders for all modes, based on a user-specified target accuracy, which is specified as the global RMS error of the fit. This feature makes use of the error estimate from the neglected eigenvalues of the potential density matrix, i.e. a multi-layer analogon of Eq. (11) (see [34] for details). When postprocessing an existing SOP fit, this target accuracy refers to the *additional* approximation introduced by MLPF. We used two options for this post-processing accuracy,  $10 \text{ cm}^{-1}$  and  $2 \text{ cm}^{-1}$ .
- FG-MLPF.** Unfortunately we were not able to perform FG-MLPF with the original grid (cf. Table 2), which contains  $11.2 \cdot 10^9$  points. Storing the PES on this grid with double-precision floating point numbers requires 84 GiB of memory, and the FG-MLPF implementation needs additional storage of similar size. To make the FG-MLPF fits feasible, we reduced the number of grid points for the  $\phi$  DOF from 21 to 15. This reduces the storage requirements for the PES to 60 GiB, making the computation possible on a single machine with 128 GiB of RAM. Again, we can choose the desired global RMS error of the FG-MLPF fit, for which we selected the three target accuracies  $10 \text{ cm}^{-1}$ ,  $2 \text{ cm}^{-1}$ , and  $0.1 \text{ cm}^{-1}$ . The latter option serves as a reference point, as it reproduces the full-grid PES almost exactly.
- RS-MLPF.** As described in Section 2.3, in addition to the target accuracy, we need to specify the oversampling parameter  $q$

for the algorithm. While the target accuracy controls the expansion orders as in FG-MLPF, the random sampling incurs an additional approximation error. This error can be reduced by increasing  $q$ , which in turn increases the runtime for the RS-MLPF algorithm. However, the size of the resulting fit depends strongly only on the target accuracy but not on  $q$ , and it is this size which is essential for the performance of the subsequent ML-MCTDH calculations. Here we explored the effects of setting  $q$  to either 2, 3, 4, or 6.

To judge the actual quality of these fits, we estimated their root-mean-square (RMS) error with respect to the original potential with a variety of sampling methods (details are given in Appendix A): uniform random sampling, Markov chain Monte Carlo, and classical molecular dynamics, where the latter two methods take an energy (or temperature) parameter for defining the Boltzmann distribution to sample over. We found that they yield very similar results at comparable temperature settings. Here we list the RMS errors obtained by molecular dynamics sampling at  $T = 600$  K (i.e.  $k_B T = 417$  cm<sup>-1</sup>), by Monte Carlo sampling at  $k_B T = 10,000$  cm<sup>-1</sup>, and by uniform random sampling (i.e. formally at  $T = \infty$ ), for all the fits that we produced. See Tables 3 and 4 for the 4-mode and the 8-mode fits, respectively. Each sample consisted of one million points; for uniform random sampling (which covers the largest region to sample over) we also performed tests with ten million sampling points, but the resulting RMS errors only differ by at most 3%, hence we conclude our sample size to be sufficient.

We observe the following noteworthy results about the fit quality:

- When comparing the original MGPF fits to those postprocessed by MLPF, we find that setting the additional fit accuracy to

2 cm<sup>-1</sup> leads to no significant change in the fit errors, even for the high-quality MGPF fit. Practically, these postprocessed fits have the same quality level as the original MGPF fits. Even when using a less accurate setting of 10 cm<sup>-1</sup> for the additional fit error, the quality of the fit is barely affected, viz. the estimated fit error is at most 1.1 cm<sup>-1</sup> higher than for the original MGPF fit.

- For FG-MLPF, the estimated global RMS error ( $T = \infty$ ) strictly observes the user-supplied accuracy parameter. This is by design, as the algorithm automatically determines the expansion order for each mode such that the user-supplied RMS threshold is not exceeded. Although this error control scheme operates using the *global* RMS error, we note that the error estimates at lower temperatures consistently lie well below this global error measure, viz. the fit errors for  $k_B T = 417$  cm<sup>-1</sup> and 10,000 cm<sup>-1</sup> lie around 30% and 60% of the global error, respectively.
- For the 4-mode RS-MLPF fits (Table 3), the global RMS error generally exceeds the prescribed accuracy parameter. This is expected, as the current error control scheme only takes into account the error caused by truncating the number of SPPs based on their natural weights, but the additional error caused by computing the optimal SPPs only approximately is not controlled for. We note that this additional error (the “RS error”) can be lowered significantly by increasing the oversampling parameter  $q$ . We find that at  $q = 6$ , the actual global RMS error lies reasonably close to the prescribed accuracy parameter (within a factor of two). Moreover, for the lower temperature settings the fit errors behave significantly better than the global error, as they appear to be much less affected by the RS error. Especially for the setting  $k_B T = 417$  cm<sup>-1</sup>, the fit error is barely worse than for FG-MLPF at the same target accuracy, even at  $q = 2$ . For  $k_B T = 10,000$  cm<sup>-1</sup>, the fit error can be brought close to the FG-MLPF result by choosing  $q = 3$  or  $q = 4$ .

**Table 3**  
Details of our 4-mode fits. The “target” column lists the accuracy parameter used for the MLPF error control. For RS-MLPF,  $q$  signifies the oversampling parameter. The number of SPPs for layers 2 and 1 are listed in the L2 and L1 columns, respectively (cf. Fig. 2). The  $k_B T$  columns list the estimated fit error at different temperature settings as described in the text.  $t_{\text{fit}}$  lists the time that it took to produce the fit.

Method	Target [cm <sup>-1</sup> ]	$q$	SPP		$k_B T$ [cm <sup>-1</sup> ]			$t_{\text{fit}}$ [s]
			L2	L1	417	10,000	$\infty$	
MGPF			14,c,22,14		8.8	20.0	60.2	
MGPF			18,c,38,18		3.7	7.9	55.0	
MGPF			23,c,56,23		1.7	3.9	54.2	
MGPF + MLPF	10.0		14,18,22,14	55,55	9.3	20.3	60.6	
MGPF + MLPF	2.0		14,32,22,14	92,92	8.8	19.8	60.2	
MGPF + MLPF	10.0		18,19,38,18	60,60	4.3	9.0	55.0	
MGPF + MLPF	2.0		18,39,38,18	110,110	3.7	7.9	55.0	
MGPF + MLPF	10.0		23,20,56,23	62,62	2.5	5.6	54.3	
MGPF + MLPF	2.0		23,43,56,23	121,121	1.7	4.0	54.3	
FG-MLPF	40.0		13,12,24,13	31,31	12.0	23.7	39.3	9573 <sup>a</sup>
FG-MLPF	10.0		18,17,38,18	53,53	2.8	5.7	9.7	9924 <sup>a</sup>
FG-MLPF	2.0		23,22,58,24	84,84	0.7	1.2	2.0	10364 <sup>a</sup>
FG-MLPF	0.1		34,33,109,35	165,165	0.03	0.06	0.10	11446 <sup>a</sup>
RS-MLPF	40.0	2	12,12,24,13	36,36	14.8	43.1	101.8	83
RS-MLPF	40.0	3	13,12,24,13	33,33	13.4	30.0	57.7	120
RS-MLPF	40.0	4	13,12,24,13	32,32	13.0	26.9	55.4	153
RS-MLPF	40.0	6	13,12,24,13	32,32	13.0	25.6	46.7	229
RS-MLPF	10.0	2	17,17,38,18	58,58	3.3	11.8	34.4	95
RS-MLPF	10.0	3	17,17,38,18	55,55	3.1	7.9	19.5	151
RS-MLPF	10.0	4	17,17,38,18	55,55	2.9	7.0	16.1	201
RS-MLPF	10.0	6	18,17,38,18	53,53	2.7	6.3	13.1	319
RS-MLPF	2.0	2	23,21,57,23	94,94	0.7	3.0	11.3	115
RS-MLPF	2.0	3	22,22,57,23	89,89	0.7	2.3	6.5	198
RS-MLPF	2.0	4	23,22,57,24	86,86	0.7	1.5	3.7	277
RS-MLPF	2.0	6	23,22,57,24	87,87	0.7	1.3	3.3	477
RS-MLPF	0.1	6	34,33,107,34	173,173	0.03	0.07	0.19	1594

<sup>a</sup> Time for fit only. Calculation of the full PES took 5183s on 16 CPU cores, but had to be performed only once for all FG-MLPF fits.

**Table 4**

Details of our 8-mode fits. Columns are as in Table 3, with an additional column L3 for the number of SPPs for layer 3 (cf. Fig. 3). For RS-MLPF,  $f_{\min}$  lists the minimum number of PES evaluations per mode.  $f$  is the actual total number of PES evaluations needed to produce the fit. Numbers in parentheses signify absolute uncertainties (one standard deviation) obtained from performing the same fit 100 times with different random seeds.

Method	Target [cm <sup>-1</sup> ]	$q$	$f_{\min}$	SPP			$k_B T$ [cm <sup>-1</sup> ]			$f/10^6$	$t_{\text{fit}}$ [s]
				L3	L2	L1	417	10,000	$\infty$		
FG-MLPF	10.0			6,6,5,7,25,13,6,6	18,17,39,18	55,55	2.8	5.6	9.8	8030.9	8889
FG-MLPF	2.0			6,7,5,8,33,15,6,7	24,22,60,24	86,86	0.7	1.2	2.0	8030.9	9044
FG-MLPF	0.1			7,8,7,10,52,15,7,8	35,34,112,36	168,168	0.03	0.06	0.10	8030.9	9526
RS-MLPF	40.0	2	0	4,5,4,5,16,8,4,5	13,11,24,12	41,41	33.6(6.4)	114.4(20)	340.4(117)	0.3	2
RS-MLPF	40.0	2	10 <sup>5</sup>	4,5,4,6,17,10,4,5	14,13,24,14	42,42	18.2(1.8)	58.6(5.6)	186.2(37)	1.5	11
RS-MLPF	40.0	3	0	4,5,4,6,16,8,4,5	12,12,24,12	38,38	23.0(2.7)	60.9(6.8)	151.9(22)	0.6	5
RS-MLPF	40.0	3	10 <sup>5</sup>	4,5,4,6,17,10,4,5	13,13,25,13	39,39	17.1(3.4)	38.4(5.7)	93.6(11)	1.9	16
RS-MLPF	40.0	6	0	4,5,4,6,17,8,4,5	12,12,24,13	35,35	18.4(1.6)	38.8(3.3)	83.3(9.4)	2.4	20
RS-MLPF	40.0	6	10 <sup>5</sup>	4,5,4,6,17,10,4,5	13,12,25,13	37,37	15.5(1.2)	28.3(1.5)	57.0(1.9)	4.0	36
RS-MLPF	10.0	2	0	5,5,5,7,23,9,5,5	17,18,38,17	64,64	8.5	35.6	108.2	1.0	10
RS-MLPF	10.0	2	10 <sup>5</sup>	6,6,5,7,23,13,6,6	19,18,39,20	64,64	4.4	19.1	70.8	2.5	23
RS-MLPF	10.0	3	0	5,6,5,7,22,9,5,6	17,16,37,17	58,58	6.2(0.9)	21.1(3.7)	60.9(14)	2.0	18
RS-MLPF	10.0	3	10 <sup>5</sup>	6,6,5,7,24,13,6,6	18,17,38,18	59,59	3.6(0.2)	10.6(0.8)	31.3(4.7)	3.9	36
RS-MLPF	10.0	4	0	6,6,4,7,23,10,6,6	17,16,37,18	58,58	4.7	14.1	38.0	3.8	35
RS-MLPF	10.0	4	10 <sup>5</sup>	6,6,5,7,23,13,6,6	18,17,37,18	57,57	3.4	8.2	18.6	5.8	52
RS-MLPF	10.0	6	0	6,6,5,7,23,11,5,6	17,17,38,18	59,59	4.1	10.6	27.0	9.6	87
RS-MLPF	10.0	6	10 <sup>5</sup>	6,6,5,7,23,13,6,6	18,17,37,18	55,55	3.3(0.3)	7.5(0.4)	16.5(0.9)	11.7	105
RS-MLPF	10.0	6	10 <sup>6</sup>	6,6,5,7,24,13,6,6	18,17,39,18	56,56	2.7	6.6	13.2	22.2	196
RS-MLPF	2.0	2	0	6,6,5,7,29,11,6,7	22,22,57,23	100,100	2.6	15.4	64.2	3.0	29
RS-MLPF	2.0	2	10 <sup>5</sup>	6,7,5,8,33,15,6,7	25,24,61,25	106,106	2.0	13.2	52.5	5.7	61
RS-MLPF	2.0	3	0	6,7,5,8,31,11,6,7	22,22,58,23	94,94	1.5	8.8	40.9	6.9	63
RS-MLPF	2.0	3	10 <sup>5</sup>	6,7,5,8,32,17,6,7	24,23,59,24	92,92	0.9	3.7	17.1	10.8	99
RS-MLPF	2.0	4	0	6,7,5,8,31,13,6,7	23,22,58,23	91,91	1.1	5.2	13.4	13.5	129
RS-MLPF	2.0	4	10 <sup>5</sup>	6,7,5,8,33,17,6,7	24,23,59,24	91,91	0.8	2.5	6.7	18.6	169
RS-MLPF	2.0	6	0	6,7,5,7,30,13,6,7	23,21,58,23	93,93	0.9	3.3	7.4	28.9	282
RS-MLPF	2.0	6	10 <sup>5</sup>	6,7,5,8,32,16,6,7	23,22,59,24	91,91	0.8(.05)	1.9(.15)	5.0(0.9)	36.3	328
RS-MLPF	2.0	6	10 <sup>6</sup>	6,7,5,8,34,17,6,7	24,23,58,24	91,91	0.7	1.6	3.5	50.7	455
RS-MLPF	0.1	6	10 <sup>6</sup>	7,8,7,10,51,21,7,8	35,34,110,35	174,174	0.03	0.09	0.24	217.2	2011
RS-MLPF	0.1	10	10 <sup>6</sup>	7,8,7,10,52,21,7,8	34,33,111,35	178,178	0.03	0.07	0.23	566.1	5114

- For the 8-mode RS-MLPF fits (Table 4), we found that the fit errors were much worse than for the 4-mode RS-MLPF fits at the same settings for target accuracy and  $q$ . Moreover, these fits finish much faster than the corresponding 4-mode fits – up to 40 times faster at low accuracy, but this advantage diminishes for higher accuracy. Both phenomena can be explained by the fact that for the 8-mode fits, most of the primitive modes are very small as they only contain a single DOF, so that even with a large  $q$  the number of PES evaluations for computing their potential density matrices is small (as low as a few hundred). This leads to a rather large RS error, which we here aim to reduce by introducing an additional parameter  $f_{\min}$  which signifies the minimum number of PES evaluations to be used when computing the potential density matrix for each mode (technically, this is done by locally adjusting  $q$  upwards). This significantly increases the fit accuracy, often by a factor of two even for  $f_{\min} = 10^5$ . For  $q = 6$  and  $f_{\min} = 10^6$  we generally reach the same level of accuracy as the 4-mode fits. The additional computation time for the fit is relatively modest, viz. several seconds (for  $f_{\min} = 10^5$ ) to a few minutes (for  $f_{\min} = 10^6$ ).
- In order to judge the reliability of the RS-MLPF method, we have repeated some of the 8-mode fits 100 times with different random seeds. The resulting average fit errors and their uncertainties (measured as the standard deviation) are recorded in Table 4. We note that with  $f_{\min} = 0$ , the relative uncertainties are rather large, often exceeding 20%. By setting  $f_{\min} \geq 10^5$ , the relative uncertainties can generally be brought down to less than 10%, especially for the fit errors at lower temperatures. This means that setting  $f_{\min}$  not only increases the accuracy of the fit, but also increases the reliability of the fit result, because

it reduces the statistical fluctuations inherent in our randomized algorithm.

- The computational resource requirements for RS-MLPF are relatively low. We stress that the RS-MLPF timings reported in Tables 3 and 4 were obtained using a single core on an Intel i5-7200U laptop CPU. Runtimes range from a few seconds to a few minutes, depending on the desired accuracy, and even the reference fits (target 0.1 cm<sup>-1</sup>) could be completed within one hour. More importantly, the memory required for running the RS-MLPF algorithm is usually less than 1 GiB – this is a major improvement over the FG-MLPF algorithm, which required about 120 GiB of RAM to run.
- The size of the RS-MLPF fits (judged by the required number of SPPs) is in general very close to the size of the corresponding FG-MLPF fit, except that for the top layer (L1), slightly more SPPs seem to be required. This phenomenon diminishes with increasing  $q$ . Hence a larger  $q$  is not only beneficial for reducing the RS error, but also makes the fit a bit more compact, which has runtime advantages for ML-MCTDH.

#### 4.3. Ground state relaxation

For all the PES fits discussed in the previous section, we have computed the ground state (i.e. zero-point) energy  $E_{\text{GS}}$  of the H<sub>3</sub>O<sub>2</sub><sup>-</sup> system. While we are interested in how the runtime for the ground state computation (performed with MCTDH or ML-MCTDH) depends on the type and the accuracy of the PES fit, we note that this runtime mostly depends on the size of the PES fit, i.e. on the number of SPPs used for each mode. Many of our PES fits, especially the RS-MLPF fits, exhibit very similar size in this

**Table 5**

Ground state energy  $E_{GS}$  and runtimes  $t_{rx}$  for the relaxation computations, using our 4-mode PES fits as defined by fit method, target accuracy, and oversampling parameter  $q$ .

Fit	Target [cm <sup>-1</sup> ]	$q$	Method <sup>a</sup>	$E_{GS}$ [cm <sup>-1</sup> ]	$t_{rx}$ [h]
<i>MGPF low (SPP = 14,c,22,14)</i>					
original			imprlx	6600.42	1.7
original			rlx,ML	6600.42	12.9
+MLPF	10.0		rlx,ML	6600.61	2.8
+MLPF	2.0		rlx,ML	6600.49	3.0
<i>MGPF medium (SPP = 18,c,38,18)</i>					
original			imprlx	6602.88	3.6
original			rlx,ML	—	32 <sup>b</sup>
<i>MGPF high (SPP = 23,c,56,23)</i>					
original			imprlx	6602.95	7.6
original			rlx,ML	—	68 <sup>b</sup>
+MLPF	10.0		rlx,ML	6602.75	3.7
+MLPF	2.0		rlx,ML	6602.94	4.0
FG-MLPF	40.0		PT,ML	6600.39	—
FG-MLPF	10.0		rlx,ML	6602.80	2.4
FG-MLPF	2.0		rlx,ML	6603.17	3.7
FG-MLPF	0.1		rlx,ML	6603.29	7.0
RS-MLPF	40.0	2	PT,ML	6604.82	—
RS-MLPF	40.0	3	PT,ML	6599.86	—
RS-MLPF	40.0	4	PT,ML	6599.05	—
RS-MLPF	40.0	6	rlx,ML	6597.86	2.0
RS-MLPF	10.0	2	PT,ML	6603.28	—
RS-MLPF	10.0	3	PT,ML	6602.79	—
RS-MLPF	10.0	4	PT,ML	6602.64	—
RS-MLPF	10.0	6	rlx,ML	6602.82	2.8
RS-MLPF	2.0	2	PT,ML	6603.14	—
RS-MLPF	2.0	3	PT,ML	6603.32	—
RS-MLPF	2.0	4	PT,ML	6603.23	—
RS-MLPF	2.0	6	rlx,ML	6603.18	3.7
RS-MLPF	0.1	6	rlx,ML	6603.29	6.7

<sup>a</sup> Method for obtaining  $E_{GS}$ : imprlx = by improved relaxation, rlx = by regular relaxation, PT = by perturbation theory (see text), ML = using ML-MCTDH.

<sup>b</sup> Estimated (see text).

regard, therefore we didn't find it necessary to perform a full relaxation run for every single one of our PES fits. Faced with limited computational resources, we instead opted to perform relaxation runs only for the most accurate RS-MLPF fits, and use the obtained ground state wavefunction to compute  $E_{GS}$  for the other, less accurate fits with a perturbation theory approach. Namely, let  $V$  be the PES fit used for computing the ground state  $\Psi_{GS}$ , and let  $\tilde{V}$  be another PES fit with its accompanying ground state  $\tilde{\Psi}_{GS}$ . Then we can estimate

$$\tilde{E}_{GS} = \langle \tilde{\Psi}_{GS} | \hat{T} + \tilde{V} | \tilde{\Psi}_{GS} \rangle \approx \langle \Psi_{GS} | \hat{T} + \tilde{V} | \Psi_{GS} \rangle \quad (38)$$

where  $\hat{T}$  denotes the kinetic energy operator. We have verified that this is a very accurate estimate by computing the GS energy for the same PES fit with all GS wavefunctions of the other fits, and found that the energies differed at most by 0.02 cm<sup>-1</sup>. The obtained GS energies and, where applicable, relaxation runtimes are listed in Tables 5 and 6 for our 4-mode and 8-mode computations, respectively. All relaxation calculations were performed on a compute node with two Intel Xeon E5-2670 CPUs, using shared memory parallelization with 16 CPU cores.

The runtime results for the relaxation calculations are summarized in Fig. 5. We elected to plot the relaxation runtime against the Monte Carlo estimated fit error at  $k_B T = 10,000$  cm<sup>-1</sup>, as this is the temperature setting which adequately covers the PES regions where the GS wavefunction has appreciable population (since  $E_{GS} \approx 6600$  cm<sup>-1</sup>). We note that the runtime for the MCTDH improved relaxation calculations with the MGPF fits (denoted by the cross symbols) increases rather rapidly with increasing fit accuracy (i.e. with decreasing fit error), whereas the runtimes for

**Table 6**

Ground state energy  $E_{GS}$  and runtimes  $t_{rx}$  for the relaxation computations, using our 8-mode PES fits as defined by fit method, target accuracy, oversampling parameter  $q$ , and minimum number of PES evaluations per mode  $f_{min}$ . Method is as in Table 5. Numbers in parentheses are uncertainties (one standard deviation) obtained by performing the same fit 100 times with different random seeds.

Fit	Target [cm <sup>-1</sup> ]	$q$	$f_{min}$	Method	$E_{GS}$ [cm <sup>-1</sup> ]	$t_{rx}$ [h]
FG-MLPF	10.0			rlx,ML	6602.45	2.3
FG-MLPF	2.0			rlx,ML	6603.10	3.4
FG-MLPF	0.1			rlx,ML	6603.29	7.5
RS-MLPF	40.0	2	0	PT,ML	6600.32(6.16)	—
RS-MLPF	40.0	2	10 <sup>5</sup>	PT,ML	6600.27(2.76)	—
RS-MLPF	40.0	3	0	PT,ML	6601.79(4.38)	—
RS-MLPF	40.0	3	10 <sup>5</sup>	PT,ML	6598.96(2.95)	—
RS-MLPF	40.0	6	0	PT,ML	6599.94(2.85)	—
RS-MLPF	40.0	6	10 <sup>5</sup>	rlx/PT,ML	6598.78(1.55)	1.4
RS-MLPF	10.0	2	0	PT,ML	6604.46	—
RS-MLPF	10.0	2	10 <sup>5</sup>	PT,ML	6603.11	—
RS-MLPF	10.0	3	0	PT,ML	6602.78(1.12)	—
RS-MLPF	10.0	3	10 <sup>5</sup>	PT,ML	6602.90(0.46)	—
RS-MLPF	10.0	4	0	PT,ML	6602.41	—
RS-MLPF	10.0	4	10 <sup>5</sup>	PT,ML	6603.02	—
RS-MLPF	10.0	6	0	PT,ML	6603.70	—
RS-MLPF	10.0	6	10 <sup>5</sup>	PT,ML	6602.43(0.40)	—
RS-MLPF	10.0	6	10 <sup>6</sup>	rlx,ML	6602.34	2.3
RS-MLPF	2.0	2	0	PT,ML	6603.02	—
RS-MLPF	2.0	2	10 <sup>5</sup>	PT,ML	6603.00	—
RS-MLPF	2.0	3	0	PT,ML	6603.35	—
RS-MLPF	2.0	3	10 <sup>5</sup>	PT,ML	6603.27	—
RS-MLPF	2.0	4	0	PT,ML	6602.97	—
RS-MLPF	2.0	4	10 <sup>5</sup>	PT,ML	6603.25	—
RS-MLPF	2.0	6	0	PT,ML	6603.21	—
RS-MLPF	2.0	6	10 <sup>5</sup>	PT,ML	6603.15(0.06)	—
RS-MLPF	2.0	6	10 <sup>6</sup>	rlx,ML	6603.13	3.6
RS-MLPF	0.1	6	10 <sup>6</sup>	PT,ML	6603.29	—
RS-MLPF	0.1	10	10 <sup>6</sup>	rlx,ML	6603.29	8.2

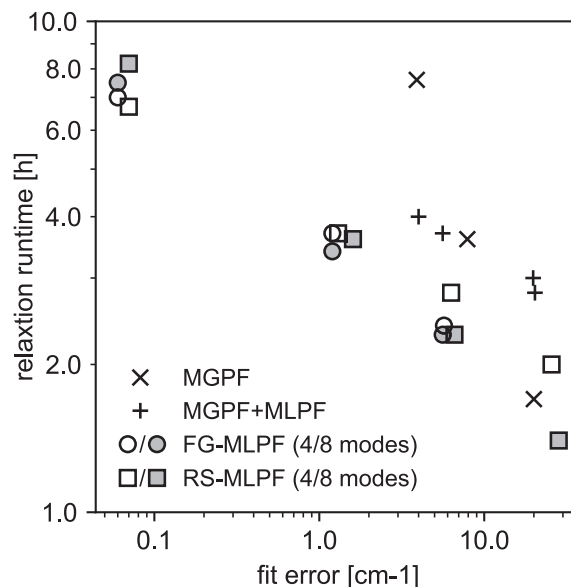


**Fig. 5.** Runtime for the relaxation calculation vs. accuracy of the PES fit. For MGPF, runtime is for the MCTDH improved relaxation run. Otherwise, runtime is for the ML-MCTDH regular relaxation run. The error of the PES fit is estimated by Metropolis-Hastings sampling over  $10^6$  points at an energy of  $k_B T = 10,000$  cm<sup>-1</sup>.

ML-MCTDH relaxations with the MLPF fits only increase moderately so; namely, using an MLPF fit that is ten times more accurate only roughly doubles the relaxation runtime. The reason for this

very different scaling behaviour between the MGPF and MLPF fits lies in the different operator format: MGPF produces fits in SOP format, while the MLPF methods produce fits in MLOp format. As discussed in Section 2.2, the SOP format necessarily requires a quickly increasing number of terms for higher accuracy fits. In [34], it was estimated that the MLOp format should lead to an asymptotically better scaling behaviour, at least under moderate assumptions for the expansion orders of the MLPF fit. Our new results fully confirm these estimations.

Furthermore, we note that postprocessing the MGPF fit by MLPF is here detrimental at low accuracy fit settings, roughly doubling the runtime for the ML-MCTDH relaxation compared to the MCTDH improved relaxation. This is mostly due to the fact that improved relaxation is algorithmically superior to regular relaxation, and due to additional overhead required by the ML-MCTDH algorithm compared to MCTDH. However at high accuracy fit settings, postprocessing the MGPF fit by MLPF becomes beneficial, roughly halving the relaxation runtime. That is, the better scaling induced by the MLOp format offsets the inferior algorithmic performance of regular relaxation compared to improved relaxation. This effect is even more pronounced when using the direct MLPF fits (i.e. FG- or RS-MLPF), which at all accuracy settings lead to better runtimes than the MLPF-postprocessed MGPF fits. Even at low fit accuracy, the direct MLPF fits lead to relaxation runtimes that can compete with the improved relaxation runtimes for the MGPF fit. This computational advantage enables us to even perform the full relaxation run for our reference PES fits (target accuracy  $0.1 \text{ cm}^{-1}$ ) in reasonable time ( $\sim 8 \text{ h}$ ). We estimate that an MGPF fit of similar accuracy would result in a runtime of well over 100 h, even with improved relaxation.

We point out that the different scaling behaviour between SOP-format (MGPF) and MLOp-format (MLPF) fits is indeed due to the different PES format, and not caused by algorithmic differences between MCTDH improved relaxation (used with the SOP fits) and ML-MCTDH regular relaxation (used with the MLOp fits). To prove this, we have performed additional ML-MCTDH relaxations with the SOP-format MGPF fits (see Table 5). Unfortunately, due to the long runtime of these computations, we were unable to perform a full 1000 fs relaxation run except for the low accuracy MGPF, and thus we estimated the full runtime by extrapolating the runtime from the partial runs. We observe that these ML-MCTDH relaxation runtimes are consistently about eight times larger than the corresponding MCTDH improved relaxation runtimes, regardless of the MGPF accuracy. That is, the SOP-format PES shows the same unfavorable scaling behaviour, independent of the relaxation method. These calculations also provide a direct measure for the computational advantage that one can gain by replacing a SOP-format PES by an MLOp-format PES with similar accuracy: namely, the ML-MCTDH computation can be sped up between  $\sim 4$  and  $\sim 20$  times when postprocessing the MGPF fit with MLPF (at negligible loss of accuracy), and the gains rapidly increase with the accuracy of the fit.

Finally, we investigate how the GS energy depends on the accuracy of the PES fit. Our results are summarized in Fig. 6, again employing the Monte Carlo error estimate at  $k_B T = 10,000 \text{ cm}^{-1}$ . Our reference PES fits consistently yield a value of  $E_{GS} = 6603.29 \text{ cm}^{-1}$ . Fits at lower accuracy deviate from this result; the lower the fit accuracy, the higher the deviation. We find that a fit error of  $\Delta V$  approximately translates to a GS energy deviation of  $\Delta E_{GS} = 0.1 \Delta V$ . Moreover, focusing on the deterministic PES fitting methods (i.e. MGPF and FG-MLPF), we observe a systematic deviation of the GS energy towards lower values. The GS energies obtained with RS-MLPF also appear to cluster at energies below the reference result, though this is partly obscured by the fluctuations induced by the random sampling, which occasionally push

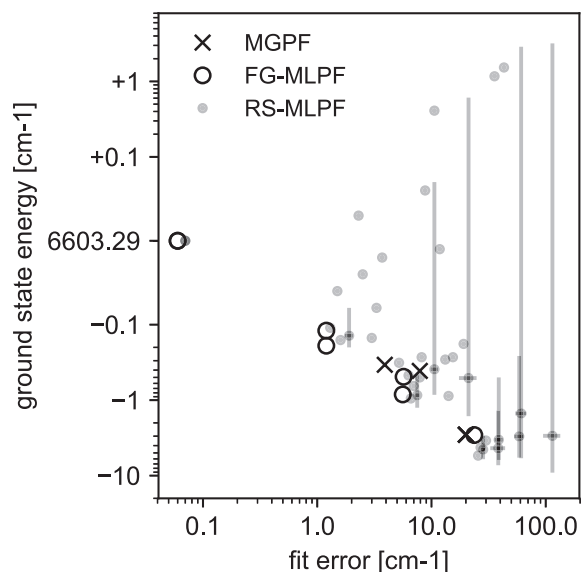


**Fig. 6.** Ground state energy (obtained by relaxation) vs. accuracy of the PES fit. Data from the RS-MLPF fits are shown by the small grey dots and, where available, their uncertainties are indicated by error bars (one standard deviation). The error of the PES fit is as in Fig. 5. Note that the GS energy axis uses linear scaling in the range  $6603.29 \pm 0.10 \text{ cm}^{-1}$  and logarithmic scaling outside this range.

$E_{GS}$  above the reference value. Currently we can not offer a satisfactory explanation for this apparently systematic deviation.

We believe that our reference result of  $E_{GS} = 6603.29 \text{ cm}^{-1}$  is fully converged to within  $0.1 \text{ cm}^{-1}$  with respect to both the PES fit accuracy and the wavefunction accuracy. However, this result holds only for the primitive basis currently used (cf. Table 2). It is likely that increasing the coordinate ranges or the number of grid points, or changing the  $d_0$  parameter, will change the value of  $E_{GS}$  by more than  $0.1 \text{ cm}^{-1}$ . Additionally, the PES itself and the electronic structure calculations which it is based on have errors that are significantly larger than the errors caused by our more accurate PES fits. Nevertheless, here we have shown that the additional fitting error that is necessary for transforming the PES into a form suitable for ML-MCTDH can be virtually eliminated completely, at least for systems with 9 DOFs.

## 5. Conclusions and outlook

We have investigated how the runtime for (ML-)MCTDH calculations depends on the accuracy of the fit for the potential energy surface (PES), using relaxation to the ground state of the  $\text{H}_3\text{O}_2^-$  system as a benchmark. While it is expected that more accurate PES fits lead to larger runtimes, we find that how strongly the runtime increases with the fit accuracy depends on the nature of the fitting method. We consistently find that PES fits in multi-layer operator (MLOp) format only lead to a modest increase of the relaxation runtimes, in contrast to PES fits in sum-of-products (SOP) format which exhibit a rather rapid increase of the relaxation runtime with the fit accuracy.

As the MLOp format can only be used with ML-MCTDH wavefunctions, we performed the corresponding ground state computations with the regular relaxation method (i.e. propagation in negative imaginary time). In contrast, fits in SOP format can be used with the improved relaxation method available for MCTDH wavefunctions, which is algorithmically superior to the regular relaxation method. Despite this algorithmic disadvantage, we find that the more favorable scaling behaviour of the MLOp fits enables

us to outperform the MCTDH improved relaxation method even at medium settings for the fit accuracy. Even with our most accurate PES fits, which were designed with a targeted global RMS error of around  $0.1 \text{ cm}^{-1}$ , the ML-MCTDH relaxation run converged with modest computational resources (less than ten hours on 16 CPU cores). Using these fits, we obtained a zero-point energy of  $6603.3 \text{ cm}^{-1}$  for the  $\text{H}_3\text{O}_2^-$  ground state. This agrees well with previously reported results of  $6605 \pm 5 \text{ cm}^{-1}$  obtained with the diffusive Monte Carlo method [71].

In order to obtain the PES fits in MLOp format, we have designed a novel variant of the multi-layer Potfit method [34] in which integrations over the full product grid are replaced by Monte Carlo integrations. The resulting method, termed “random sampling multi-layer Potfit” (RS-MLPF), produces PES fits that are parametrized by a target accuracy (for the global root-mean-square error) and an oversampling parameter  $q$  which controls the number of PES evaluations used for the Monte Carlo integrations. Using a prototype implementation of RS-MLPF, we have produced a large number of PES fits to investigate how its accuracy depends on these parameters, where the actual fit accuracy was assessed via Monte Carlo as well as molecular dynamics sampling methods. Compared to the original “full-grid” MLPF, RS-MLPF requires much less computational resources (only a single CPU core and less than 1 GiB of RAM), but produces larger fit errors due to additional errors from the random sampling. Hence an RS-MLPF fit will usually miss the prescribed target accuracy, though we found that setting a large enough  $q$  (e.g.  $q = 3$  or  $4$ ) brings the fit error down to below twice the target accuracy, thus enabling us to produce PES fits with good *a priori* estimates for its accuracy. However, we observed that RS-MLPF occasionally needs some additional tuning regarding the number of PES evaluations used, and further investigations on other and larger systems will be needed to develop fully reliable heuristics for choosing the parameters of the method.

For the 9-dimensional system under study here, the RS-MLPF method allows us to produce PES fits that are virtually exact, i.e. their fit error is tiny (much below  $1 \text{ cm}^{-1}$ ) compared to the actual accuracy of the PES. Moreover, these PES fits can be obtained with modest computational resources, and they are fully usable with ML-MCTDH, as they don't cause excessive runtimes for the relaxation or propagation. These features make us very optimistic that the method will be applicable to larger systems with up to about 20 DOFs. While we don't expect to be able to reproduce the extreme level of accuracy which we obtained for the 9D system here, fits with good accuracy (i.e. below  $\sim 10 \text{ cm}^{-1}$  in the low-energy region) seem to be in reach with RS-MLPF, though additional work regarding its implementation (especially parallelisation) will be required. The combination of RS-MLPF and ML-MCTDH will thus yield a method for quantum molecular dynamics on general potential energy surfaces with unprecedented accuracy and performance.

## Acknowledgements

This research did not receive any specific grant from funding agencies in the public, commercial, or not-for-profit sectors. Part of this research was carried out while the authors were at the Theoretical Chemistry Group, Institute for Physical Chemistry, University of Heidelberg, Germany. We gratefully acknowledge the use of their computational facilities for performing the MGPF and the FG-MLPF fits. The majority of the relaxation calculations were performed on computational facilities kindly provided by the Computational Biophysics group of Prof. Wang Yi at the Chinese University of Hong Kong. FO thanks Markus Schröder for discussing algorithmic details of the Monte-Carlo Potfit approach. Finally, the authors would like to thank Hans-Dieter Meyer for his continuous

friendship, advice and support in scientific as well as in personal matters.

## Appendix A. Estimating the PES fitting error

The root-mean-square (rms) error of the potential fit  $\tilde{V}(q)$  with respect to the original potential  $V(q)$  is given by

$$\Delta_{\text{rms}}V = \left[ \int dq w(q) (\tilde{V}(q) - V(q))^2 \right]^{1/2} \quad (\text{A.1})$$

where  $w(q)$  is a weight function, which is non-negative and fulfills  $\int dq w(q) = 1$ . Replacing the integral by a summation over *all* grid points results in an expression that is too expensive to evaluate, due to the enormous size of the full product grid. To estimate the rms error, the integral is instead replaced by a summation over a *sample* of grid points,  $S = \{q_i | 1 \leq i \leq N\}$ , where the samples are drawn according to the probability distribution  $w(q)$ .

To assess the global accuracy of the fit, we employ uniform random sampling, i.e. all grid points are equally likely to be sampled, corresponding to  $w(q) = \text{const}$ . Alternatively, to assess the accuracy of the fit in a specific energy region, we gather the sample  $S$  from a Boltzmann distribution, i.e. using

$$w(q) = \exp(-\beta V(q)) / \int dq' \exp(-\beta V(q')) \quad (\text{A.2})$$

where  $\beta = 1/k_B T$  depends on a temperature parameter  $T$ , and  $k_B$  denotes the Boltzmann constant.

The Boltzmann sampling can be performed using a Markov chain Monte Carlo (MCMC) approach with the Metropolis-Hastings algorithm [63,64]. For the 9D system under study here, this approach works adequately. However, for larger dimensionality it is known that this algorithm performs more and more poorly, as the random walkers which are used to explore the conformation space take more and more time to cover the relevant region defined by the probability distribution, hence it becomes difficult to reach satisfactory accuracy. As an alternative to the MCMC approach, we here introduce the option of performing the Boltzmann sampling by using classical molecular dynamics (MD), which has become the standard approach for sampling complex systems with higher dimensionality, such as proteins or membranes [73].

To perform the MD simulations, we employed the standard MD package NAMD [74] where we overrode the standard calculation of the atomic forces with a finite difference gradient of the PES3C potential (since the PES3C routine doesn't offer analytical gradients). Starting from the potential minimum as the initial conformation, we simulated an NVT ensemble using the Langevin thermostat [75] for one million steps. Note that the PES3C potential is invariant with respect to permutations of the hydrogen or the oxygen atoms, and NAMD preserves this invariance as the MD simulation is carried out in Cartesian coordinates. However, our PES fit is given in internal coordinates, which do not obey the permutational invariance. Therefore, when transforming the conformations generated by NAMD from Cartesian to internal coordinates, we must make a choice for assigning the three hydrogens according to the definition of the internal coordinates (see Fig. 1). Our choice was done as follows: First, for each oxygen, find the hydrogen closest to it. This defines the two OH moieties. Then, the remaining hydrogen is defined as the bridging H. We found that such an assignment was always possible for all the conformations generated by the MD simulation. After the transformation to internal coordinates, each conformation was replaced by the nearest conformation on the product grid, as our PES fits are strictly only defined on the grid points. It was necessary to drop a small number of conformations which came to lie outside the coordinate ranges given in Table 2.

As a remark, we note that the thermostat does not fix the system temperature always at a given value, but rather keeps the average temperature around the given value. That is, the instantaneous temperature always fluctuates around the desired value. Due to the small system size (only 5 atoms) this fluctuations can be large, but the average temperature is well maintained around the prescribed value. For instance, we performed an MD simulation with a prescribed  $T = 300$  K which yielded an averaged temperature of  $\bar{T} = 300.1$  K with a standard deviation of  $\Delta T = 109$  K. Similar behaviour was found for  $T = 600$  K and  $T = 1000$  K, with observed temperatures of  $598 \pm 219$  K and  $1008 \pm 366$  K, respectively. Nevertheless, when comparing the MD  $T = 600$  K error estimates for our PES fits with the MCMC estimates at a comparable temperature setting ( $k_B T = 400$  cm<sup>-1</sup>, i.e.  $T = 576$  K), we found very good agreement throughout. Hence we conclude that the MD error estimate is a viable alternative to the MCMC approach, and is likely to work even in rather large dimensionality.

## References

- [1] G.A. Worth, L.S. Cederbaum, Beyond Born-Oppenheimer: conical intersections and their impact on molecular dynamics, *Ann. Rev. Phys. Chem.* 55 (2004) 127–158.
- [2] G.A. Worth, M.A. Robb, I. Burghardt, A novel algorithm for non-adiabatic direct dynamics using variational Gaussian wavepackets, *Faraday Discuss.* 127 (2004) 307–323.
- [3] G.A. Worth, M.A. Robb, B. Lasorne, Solving the time-dependent Schrödinger equation for nuclear motion in one step: direct dynamics of non-adiabatic systems, *Mol. Phys.* 106 (2008) 2077–2091.
- [4] H.-D. Meyer, U. Manthe, L.S. Cederbaum, The multi-configurational time-dependent Hartree approach, *Chem. Phys. Lett.* 165 (1990) 73–78.
- [5] M.H. Beck, A. Jäckle, G.A. Worth, H.-D. Meyer, The multiconfiguration time-dependent Hartree method: a highly efficient algorithm for propagating wavepackets, *Phys. Rep.* 324 (2000) 1–105.
- [6] H.-D. Meyer, F. Gatti, G.A. Worth (Eds.), *Multidimensional Quantum Dynamics: MCTDH Theory and Applications*, Wiley-VCH, Weinheim, 2009.
- [7] H.-D. Meyer, Studying molecular quantum dynamics with the multiconfiguration time-dependent Hartree method, *Wiley Interdisciplinary Rev.: Comput. Mol. Sci.* 2 (2012) 351.
- [8] A. Raab, G. Worth, H.-D. Meyer, L.S. Cederbaum, Molecular dynamics of pyrazine after excitation to the  $S_2$  electronic state using a realistic 24-mode model Hamiltonian, *J. Chem. Phys.* 110 (1999) 936–946.
- [9] C. Cattarius, G.A. Worth, H.-D. Meyer, L.S. Cederbaum, All mode dynamics at the conical intersection of an octa-atomic molecule: multi-configuration time-dependent Hartree (MCTDH) investigation on the butatriene cation, *J. Chem. Phys.* 115 (2001) 2088–2100.
- [10] F. Gatti, F. Otto, S. Sukiasyan, H.-D. Meyer, Rotational excitation cross sections of *para*-H<sub>2</sub> + *para*-H<sub>2</sub> collisions. A full-dimensional wave packet propagation study using an exact form of the kinetic energy, *J. Chem. Phys.* 123 (2005) 174311.
- [11] O. Vendrell, F. Gatti, H.-D. Meyer, Full dimensional (15D) quantum-dynamical simulation of the protonated water dimer II: infrared spectrum and vibrational dynamics, *J. Chem. Phys.* 127 (2007) 184303.
- [12] O. Vendrell, H.-D. Meyer, A proton between two waters: insight from full-dimensional quantum-dynamics simulations of the [H<sub>2</sub>O-H-OH<sub>2</sub>]<sup>+</sup> cluster, *PCCP* 10 (2008) 4692–4703.
- [13] F. Otto, F. Gatti, H.-D. Meyer, Rotational excitations in *para*-H<sub>2</sub> + *para*-H<sub>2</sub> collisions: full- and reduced-dimensional quantum wave packet studies comparing different potential energy surfaces, *J. Chem. Phys.* 128 (2008) 064305.
- [14] F. Otto, F. Gatti, H.-D. Meyer, Rovibrational energy transfer in collisions of H<sub>2</sub> with D<sub>2</sub>. A full-dimensional wave packet propagation study, *Mol. Phys.* 110 (2012) 619.
- [15] A. Markmann, G. Worth, S. Mahapatra, H.-D. Meyer, H. Köppel, L. Cederbaum, Simulation of a complex spectrum: interplay of five electronic states and 21 vibrational degrees of freedom in C<sub>2</sub>H<sub>4</sub><sup>+</sup>, *J. Chem. Phys.* 123 (2005) 204310.
- [16] O. Vendrell, F. Gatti, D. Lauvergnat, H.-D. Meyer, Full dimensional (15D) quantum-dynamical simulation of the protonated water dimer I: Hamiltonian setup and analysis of the ground vibrational state, *J. Chem. Phys.* 127 (2007) 184302.
- [17] O. Vendrell, M. Brill, F. Gatti, D. Lauvergnat, H.-D. Meyer, Full dimensional (15D) quantum-dynamical simulation of the protonated water dimer III: mixed Jacobi-valence parametrization and benchmark results for the zero-point energy, vibrationally excited states and infrared spectrum, *J. Chem. Phys.* 130 (2009) 234305.
- [18] M. Schröder, F. Gatti, H.-D. Meyer, Theoretical studies of the tunneling splitting of malonaldehyde using the multiconfiguration time-dependent Hartree approach, *J. Chem. Phys.* 134 (2011) 234307.
- [19] M. Schröder, H.-D. Meyer, Calculation of the vibrational excited states of malonaldehyde and their tunneling splittings with the multi-configuration time-dependent Hartree method, *J. Chem. Phys.* 141 (2014) 034116.
- [20] K. Sadri, D. Lauvergnat, F. Gatti, H.-D. Meyer, Rovibrational spectroscopy using a kinetic energy operator in Eckart frame and the multi-configuration time-dependent Hartree (MCTDH) approach, *J. Chem. Phys.* 141 (2014) 114101.
- [21] D. Peláez, K. Sadri, H.-D. Meyer, Full-dimensional MCTDH/MGPF study of the ground and lowest lying vibrational states of the bihydroxide H<sub>3</sub>O<sub>2</sub><sup>-</sup> complex, *Spectrochimica Acta Part A* 119 (2014) 42–51.
- [22] D. Peláez, H.-D. Meyer, On the infrared absorption spectrum of the hydrated hydroxide (H<sub>3</sub>O<sub>2</sub><sup>-</sup>) cluster anion, *Chem. Phys.* 482 (2017) 100–105.
- [23] H. Wang, M. Thoss, Multilayer formulation of the multiconfiguration time-dependent Hartree theory, *J. Chem. Phys.* 119 (2003) 1289–1299.
- [24] U. Manthe, A multilayer multiconfigurational time-dependent Hartree approach for quantum dynamics on general potential energy surfaces, *J. Chem. Phys.* 128 (2008) 164116.
- [25] O. Vendrell, H.-D. Meyer, Multilayer multiconfiguration time-dependent Hartree method: implementation and applications to a Henon-Heiles Hamiltonian and to pyrazine, *J. Chem. Phys.* 134 (2011) 044135.
- [26] I.R. Craig, H. Wang, M. Thoss, Proton transfer reactions in model condensed-phase environments: accurate quantum dynamics using the multilayer multiconfiguration time-dependent Hartree approach, *J. Chem. Phys.* 127 (2007) 144503.
- [27] H. Wang, M. Thoss, From coherent motion to localization: II. Dynamics of the spin-boson model with sub-Ohmic spectral density at zero temperature, *Chem. Phys.* 370 (2010) 78–86.
- [28] T. Westermann, R. Brodbeck, A.B. Rozhenko, W. Schoeller, U. Manthe, Photodissociation of methyl iodide embedded in a host-guest complex: a full dimensional (189D) quantum dynamics study of CH<sub>3</sub>@resor[4]arene, *J. Chem. Phys.* 135 (2011) 184102.
- [29] R. Welsch, U. Manthe, Reaction dynamics with the multi-layer multiconfigurational time-dependent Hartree approach: H + CH<sub>4</sub> → H<sub>2</sub> + CH<sub>3</sub> rate constants for different potentials, *J. Chem. Phys.* 137 (2012) 244106.
- [30] I.R. Craig, M. Thoss, H. Wang, Accurate quantum-mechanical rate constants for a linear response Azzouz-Borgis proton transfer model employing the multilayer multiconfiguration time-dependent Hartree approach, *J. Chem. Phys.* 135 (2011), 064504.
- [31] Q. Meng, S. Faraji, O. Vendrell, H.-D. Meyer, Full dimensional quantum-mechanical simulations for the vibronic dynamics of difluorobenzene radical cation isomers using the multilayer multiconfiguration time-dependent Hartree method, *J. Chem. Phys.* 137 (2012) 134302.
- [32] Q. Meng, H.-D. Meyer, A multilayer MCTDH study on the full dimensional vibronic dynamics of naphthalene and anthracene cations, *J. Chem. Phys.* 138 (2013), 014313.
- [33] Y. Xie, J. Zheng, Z. Lan, Full-dimensional multilayer multiconfigurational time-dependent Hartree study of electron transfer dynamics in the anthracene/C60 complex, *J. Chem. Phys.* 142 (2015), 084706.
- [34] F. Otto, Multi-layer Potfit: an accurate potential representation for efficient high-dimensional quantum dynamics, *J. Chem. Phys.* 140 (2014), 014106.
- [35] U. Manthe, A time-dependent discrete variable representation for (multi-configuration) Hartree methods, *J. Chem. Phys.* 105 (1996) 6989.
- [36] U. Manthe, Layered discrete variable representations and their application within the multiconfigurational time-dependent Hartree approach, *J. Chem. Phys.* 130 (2009), 054109.
- [37] R. Welsch, U. Manthe, Fast Shepard interpolation on graphics processing units: potential energy surfaces and dynamics for H + CH<sub>4</sub> → H<sub>2</sub> + CH<sub>3</sub>, *J. Chem. Phys.* 138 (2013) 164118.
- [38] S. Manzhos, T. Carrington Jr., A random-sampling high dimensional model representation neural network for building potential energy surfaces, *J. Chem. Phys.* 125 (2006), 084109.
- [39] E. Pradhan, J.-L. Carren-Macedo, J.E. Cuervo, M. Schröder, A. Brown, Ab Initio potential energy and dipole moment surfaces for CS<sub>2</sub>: determination of molecular vibrational energies, *J. Phys. Chem. A* 117 (2013) 6925–6931.
- [40] S. Manzhos, R. Dawes, T. Carrington, Neural network-based approaches for building high dimensional and quantum dynamics-friendly potential energy surfaces, *Int. J. Quantum Chem.* 115 (2015) 1012–1020.
- [41] E. Pradhan, A. Brown, A ground state potential energy surface for HONO based on a neural network with exponential fitting functions, *Phys. Chem. Chem. Phys.* 19 (2017) 22272–22281.
- [42] A. Brown, E. Pradhan, Fitting potential energy surfaces to sum-of-products form with neural networks using exponential neurons, *J. Theor. Comput. Chem.* 16 (2017) 1730001.
- [43] S. Carter, S.J. Culik, J.M. Bowman, Vibrational self-consistent field method for many-mode systems: A new approach and application to the vibrations of CO adsorbed on Cu(100), *J. Chem. Phys.* 107 (1997) 10458.
- [44] H. Rabitz, O.F. Alis, General foundations of high-dimensional model representations, *J. Math. Chem.* 25 (1999) 197.
- [45] O. Vendrell, F. Gatti, H.-D. Meyer, Dynamics and infrared spectroscopy of the protonated water dimer, *Angew. Chem. Int. Ed.* 46 (2007) 6918–6921.
- [46] O. Vendrell, F. Gatti, H.-D. Meyer, Full dimensional (15D) quantum-dynamical simulation of the protonated water dimer IV: Isotope effects in the infrared spectra of D(D<sub>2</sub>O)<sub>2</sub><sup>+</sup>, H(D<sub>2</sub>O)<sub>2</sub><sup>+</sup> and D(H<sub>2</sub>O)<sub>2</sub><sup>+</sup> isotopologues, *J. Chem. Phys.* 131 (2009) 034308.
- [47] S. Manzhos, T. Carrington, Using neural networks, optimized coordinates, and high-dimensional model representations to obtain a vinyl bromide potential surface, *J. Chem. Phys.* 129 (2008) 224104.

- [48] G.-J. Kroes, H.-D. Meyer, Using  $n$ -mode potentials for reactive scattering: application to 6D  $H_2 + Pt(111)$ , *Chem. Phys. Lett.* 440 (2007) 334–340.
- [49] A. Jäckle, H.-D. Meyer, Product representation of potential energy surfaces, *J. Chem. Phys.* 104 (1996) 7974.
- [50] L.R. Tucker, Implications of factor analysis of three-way matrices for measurements of change, in: C.W. Harris (Ed.), *Problems in Measuring Change*, University of Wisconsin Press, Madison, 1963, pp. 122–137.
- [51] D. Peláez, H.-D. Meyer, The multigrid POTFIT (MGPF) method: grid representations of potentials for quantum dynamics of large systems, *J. Chem. Phys.* 138 (2013) 014108.
- [52] M. Schröder, H.-D. Meyer, Transforming high-dimensional potential energy surfaces into sum-of-products form using Monte Carlo methods, *J. Chem. Phys.* 147 (2017) 064105.
- [53] L. Grasedyck, Hierarchical singular value decomposition of tensors, *SIAM J. Matrix Anal. Appl.* 31 (2010) 2029–2054.
- [54] P.A.M. Dirac, Note on exchange phenomena in the Thomas atom, *Proc. Cambridge Philos. Soc.* 26 (1930) 376–385.
- [55] J. Frenkel, *Wave Mechanics*, Clarendon Press, Oxford, 1934.
- [56] R. Kosloff, H. Tal-Ezer, A direct relaxation method for calculating eigenfunctions and eigenvalues of the Schrödinger equation on a grid, *Chem. Phys. Lett.* 127 (1986) 223.
- [57] H.-D. Meyer, F. Le Quéré, C. Léonard, F. Gatti, Calculation and selective population of vibrational levels with the Multiconfiguration Time-Dependent Hartree (MCTDH) algorithm, *Chem. Phys.* 329 (2006) 179–192.
- [58] L.J. Doriol, F. Gatti, C. lung, H.-D. Meyer, Computation of vibrational energy levels and eigenstates of fluoroform using the multiconfiguration time-dependent Hartree method, *J. Chem. Phys.* 129 (2008) 224109.
- [59] G.A. Worth, M.H. Beck, A. Jäckle, O. Vendrell, H.-D. Meyer, The Heidelberg MCTDH Package, version 8.5, 2011–2017, URL: <http://mctdh.uni-hd.de/>.
- [60] H. Wang, Multilayer multiconfiguration time-dependent Hartree theory, *J. Phys. Chem. A* 119 (2015) 7951.
- [61] F. Gatti, C. lung, Exact and constrained kinetic energy operators for polyatomic molecules: the polyspherical approach, *Phys. Rep.* 484 (2009) 1–69.
- [62] L.D. Lathauwer, B.D. Moor, J. Vandewalle, A multilinear singular value decomposition, *SIAM J. Matrix Anal. Appl.* 21 (2000) 1253–1278.
- [63] N. Metropolis, A.W. Rosenbluth, M.N. Rosenbluth, A.H. Teller, E. Teller, Equation of state calculations by fast computing machines, *J. Chem. Phys.* 21 (1953) 1087–1092.
- [64] W.K. Hastings, Monte Carlo sampling methods using Markov chains and their applications, *Biometrika* 57 (1970) 97–109.
- [65] J. Bezanson, A. Edelman, S. Karpinski, V.B. Shah, Julia: a fresh approach to numerical computing, *SIAM Rev.* 59 (2017) 65–98.
- [66] M.E. Tuckerman, D. Marx, M.L. Klein, M. Parrinello, On the quantum nature of the shared proton in hydrogen bonds, *Science* 275 (1997) 817–820.
- [67] M.E. Tuckerman, D. Marx, M. Parrinello, The nature and transport mechanism of hydrated hydroxide ions in aqueous solution, *Nature* 417 (2002) 925–929.
- [68] X. Huang, B.J. Braams, S. Carter, J.M. Bowman, Quantum calculations of vibrational energies of  $H_3O_2^-$  on an ab initio potential, *J. Am. Chem. Soc.* 126 (2004) 5042–5043.
- [69] E.G. Diken, J.M. Headrick, J.R. Roscioli, J.C. Bopp, M.A. Johnson, A.B. McCoy, Fundamental excitations of the shared proton in the  $H_3O_2^-$  and  $H_5O_2^+$  complexes, *J. Phys. Chem. A* 109 (2005) 1487–1490.
- [70] H.-G. Yu, A rigorous full-dimensional quantum dynamics calculation of the vibrational energies of  $H_3O_2^-$ , *J. Chem. Phys.* 125 (2006) 204306.
- [71] A.B. McCoy, X. Huang, S. Carter, J.M. Bowman, Quantum studies of the vibrations in  $H_3O_2^-$  and  $D_3O_2^-$ , *J. Chem. Phys.* 123 (2005) 064317.
- [72] M. Ndong, L. Joubert Doriol, H.-D. Meyer, A. Nauts, F. Gatti, D. Lauvergnat, Automatic computer procedure for generating exact and analytical kinetic energy operators based on the polyspherical approach, *J. Chem. Phys.* 136 (2012) 034107.
- [73] D.E. Shaw, P. Maragakis, K. Lindorff-Larsen, S. Piana, R.O. Dror, M.P. Eastwood, J.A. Bank, J.M. Jumper, J.K. Salmon, Y. Shan, W. Wriggers, Atomic-level characterization of the structural dynamics of proteins, *Science* 330 (2010) 341–346.
- [74] J.C. Phillips, R. Braun, W. Wang, J. Gumbart, E. Tajkhorshid, E. Villa, C. Chipot, R. D. Skeel, L. Kalé, K. Schulten, Scalable molecular dynamics with NAMD, *J. Comput. Chem.* 26 (2005) 1781–1802.
- [75] G.S. Grest, K. Kremer, Molecular dynamics simulation for polymers in the presence of a heat bath, *Phys. Rev. A* 33 (1986) 3628–3631.